

Fall 2006

An experimental study on the buoyancy-driven motion of air bubbles in square channels

Vinod Bulusu

University of New Hampshire, Durham

Follow this and additional works at: <https://scholars.unh.edu/thesis>

Recommended Citation

Bulusu, Vinod, "An experimental study on the buoyancy-driven motion of air bubbles in square channels" (2006). *Master's Theses and Capstones*. 194.

<https://scholars.unh.edu/thesis/194>

This Thesis is brought to you for free and open access by the Student Scholarship at University of New Hampshire Scholars' Repository. It has been accepted for inclusion in Master's Theses and Capstones by an authorized administrator of University of New Hampshire Scholars' Repository. For more information, please contact nicole.hentz@unh.edu.

**AN EXPERIMENTAL STUDY ON THE BUOYANCY-
DRIVEN MOTION OF AIR BUBBLES IN SQUARE
CHANNELS**

BY

VINOD BULUSU

B.S., Chemical Engineering, Andhra University, 2003

THESIS

Submitted to the University of New Hampshire

in Partial Fulfillment of the

Requirements for the Degree of

Masters of Science

in

Chemical Engineering

September 2006

UMI Number: 1437620

Copyright 2006 by
Bulusu, Vinod

All rights reserved.

INFORMATION TO USERS

The quality of this reproduction is dependent upon the quality of the copy submitted. Broken or indistinct print, colored or poor quality illustrations and photographs, print bleed-through, substandard margins, and improper alignment can adversely affect reproduction.

In the unlikely event that the author did not send a complete manuscript and there are missing pages, these will be noted. Also, if unauthorized copyright material had to be removed, a note will indicate the deletion.

UMI[®]

UMI Microform 1437620

Copyright 2006 by ProQuest Information and Learning Company.

All rights reserved. This microform edition is protected against unauthorized copying under Title 17, United States Code.

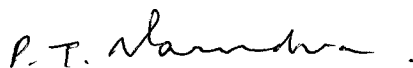
ProQuest Information and Learning Company
300 North Zeeb Road
P.O. Box 1346
Ann Arbor, MI 48106-1346

This dissertation has been examined and approved.



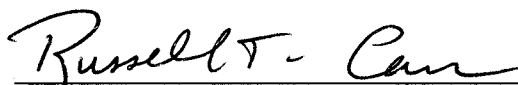
Thesis Director, Nivedita R. Gupta

Assistant Professor of Chemical Engineering



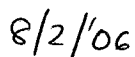
Palligarnai T. Vasudevan

Professor of Chemical Engineering



Russell T. Carr

Professor of Chemical Engineering



Date

DEDICATION

To Amma, Nanna and Madhuri

ACKNOWLEDGEMENTS

I would like to thank my thesis advisor, Dr. Nivedita Gupta, without whose guidance and initiative I could never have finished my Masters thesis. I would like to thank Dr. P.T. Vasudevan and Dr. R.T. Carr for taking the time to be on my thesis committee.

I also want to express my gratitude to Dr. S.S.T. Fan, Chair of the Department of the Chemical Engineering for his great help during the past three years. I would like to thank Mr. Jonathan E. Newell for his assistance with customized capillaries. I would like to thank Mr. Eric C Beauregard and Michael O' Connor for their support and help while working at Interfacial Phenomena lab. I also want to thank Malvern Instruments, for their cooperation in determining the fluid properties.

Finally, I would like to thank all my friends for their support and motivation in finishing my thesis.

TABLE OF CONTENTS

DEDICATION.....	iii
ACKNOWLEDGEMENT.....	iv
LIST OF TABLES.....	vii
LIST OF FIGURES.....	viii
ABSTRACT.....	xiii

CHAPTER	PAGE
I INTRODUCTION.....	1
Newtonian Systems.....	3
Viscoelastic Systems.....	4
Surfactant Systems.....	7
Objectives.....	9
II BACKGROUND.....	11
Newtonian Systems.....	11
Viscoelastic Systems.....	18
Surfactant Systems.....	22

III	EXPERIMENTAL METHODS.....	25
	Experimental Setup.....	25
	Experimental Procedure.....	27
	Materials and Methods.....	28
	Material Properties.....	35
IV	RESULTS AND DISCUSSION.....	41
	Newtonian Systems.....	42
	Viscoelastic Systems.....	60
	Surfactant Systems.....	67
V	SUMMARY AND FUTURE WORK.....	74
	REFERENCES.....	77
	APPENDIX	
	C-program to calculate the bubble volume from r-z data.....	81

LIST OF TABLES

TABLE	PAGE
3.1 Properties of the chemicals used in the experiment.....	29
3.2 Material properties of Newtonian fluid systems studied.....	38
3.3 Material properties of viscoelastic fluid systems studied.....	39
3.4 Material properties of surfactant systems studied.....	39
3.5 Dimensionless values of parameters in the experiment.....	40

LIST OF FIGURES

FIGURE	PAGE
1.1 Rod-climbing phenomena observed in a viscoelastic fluid when a rod is rotated in a beaker filled with (a) Newtonian fluid and (b) viscoelastic fluid.....	5
1.2 Die-swelling phenomena observed in a viscoelastic fluid as a free jet of (a) Newtonian fluid and (b) viscoelastic fluid flows out of a capillary tube.....	6
1.3 Schematic of the two-dimensional cusp shapes observed for motion of air bubbles in a capillary filled with viscoelastic fluid.....	7
3.1 Schematic of the experimental setup used to study the buoyancy-driven motion of bubbles in square channel.....	26
3.2 Steady shear viscosity as a function of the shear rate for the viscoelastic fluids used in the experiments.....	31
3.3 Storage modulus (G') and loss modulus (G'') as a function of the shear strain for 0.1 % PAM solution in water.....	33
3.4 Storage modulus (G') and loss modulus (G'') as a function of the shear strain for 0.25 % PAM solution in water.....	33
3.5 Storage modulus (G') and loss modulus (G'') as a function of the shear strain for 0.1 % PAM solution in 50 % glycerol-water solution.....	34
3.6 Equilibrium surface tension as a function of Triton X-100 concentration in 95% glycerol-water solution.....	35
3.7 Schematic of front view and cross-section view of a bubble rising in a square channel. The bubble maybe (a) axisymmetric or (b) non-axisymmetric in the cross-section view.....	37

4.1	Terminal velocity as a function of the bubble volume for air bubbles rising in 80% glycerol-water solution in 10mm square capillary.....	42
4.2	Steady shapes as a function of the dimensionless bubble size for air bubbles rising in 90% glycerol-water solution in 15 mm square capillary ($Bo = 11.83$).....	43
4.3	The (a) length and (b) width of bubbles as a function of bubble size for bubbles rising in 90% glycerol-water solution in 15 mm square capillary.....	44
4.4	The length of the bubble as a function of the bubble width for bubbles rising in 90% glycerol-water solution in 15 mm square capillary.....	45
4.5	The deformation parameter as a function of the dimensionless bubble size for bubbles rising in 90% glycerol-water solution in 15 mm square capillary.....	46
4.6	The dimensionless film thickness as a function of the dimensionless bubble size for bubbles rising in 90% glycerol-water solution in 15 mm square capillary.....	46
4.7	Terminal velocity as a function of the bubble volume for air bubbles rising in 90% glycerol-water solution in 15 mm square capillary.....	48
4.8	Dimensionless terminal velocity as a function of the dimensionless bubble size for air bubbles rising in 90% glycerol-water solution in 15 mm square capillary.....	48
4.9	Steady dimensionless velocity of air bubbles as a function of the dimensionless bubble size for air bubbles rising in 90% glycerol-water solution in 15 mm square capillary.....	49
4.10	Steady shapes for air bubbles as a function of the dimensionless bubble size for air bubbles rising in GW1-2, GW2-2, GW3-2, and GW4-2 systems.....	50
4.11	The (a) length and (b) width of bubbles as a function of bubble size for bubbles rising in 80%, 90%, and 99% glycerol-water solution in 15 mm square capillary.....	51

4.12	Comparison of the length of the bubble as a function of the bubble width for bubbles rising in 80%, 90%, and 99% glycerol-water solutions in 15 mm square capillary.....	52
4.13	Comparison of the deformation parameter as a function of the dimensionless bubble size for bubbles rising in 80%, 90%, and 99% glycerol-water solutions in 15 mm square capillary.....	53
4.14	Comparison of the dimensionless film thickness as a function of the bubble size for bubbles rising in 80%, 90%, and 99% glycerol-water solutions in a 15 mm square capillary.....	54
4.15	Comparison of terminal velocity as a function of the bubble volume for air bubbles rising in 80%, 90%, and 95% glycerol-water solution in 15 mm square capillary.....	55
4.16	Comparison of dimensionless terminal velocity as a function of the bubble size for air bubbles rising in 80%, 90%, and 99% glycerol-water solutions in 15 mm square capillary.....	55
4.17	Comparison of steady dimensionless velocity of air bubbles as a function of the bubble size for air bubbles rising in 80%, 90%, and 99% glycerol-water solution in 15 mm square capillary.....	56
4.18	Steady shapes as a function of the dimensionless bubble size for GW1-1 system with bubbles showing no reentrant cavity.....	57
4.19	Unsteady shapes for varying bubble sizes for air bubbles rising in water showing a reentrant cavity.....	57
4.20	Steady bubble shapes as a function of the dimensionless bubble size for GW4-3 with bubbles showing a reentrant cavity.....	58
4.21	Comparison of terminal velocity as a function of the bubble volume for air bubbles rising in 80% glycerol-water solution in 10 mm and 15 mm square capillary.....	59
4.22	Steady bubble shapes as a function of the dimensionless bubble size for GW1-1 and GW1-2 systems.....	59

4.23	Steady shapes as a function of the dimensionless bubble size for air bubbles rising in 0.1% PAM solution in 15 mm square capillary ($Bo = 7.71$).....	60
4.24	The (a) length and (b) width of bubbles as a function of bubble size for bubbles rising in 0.1% PAM solution in 15 mm square capillary.....	61
4.25	The length of the bubble as a function of the bubble width for bubbles rising in 0.1% PAM solution in 15 mm square capillary.....	62
4.26	The deformation parameter as a function of the dimensionless bubble size for bubbles rising in 0.1% PAM solution in 15 mm square capillary.....	62
4.27	The dimensionless film thickness as a function of the dimensionless bubble size for bubbles rising in 0.1% PAM solution in 15 mm square capillary.....	63
4.28	Steady shapes for air bubbles as a function of the dimensionless bubble size for air bubbles rising in 0.1% PAM, 0.25% PAM, and 0.1% PAM in 50% glycerol-water solutions.....	65
4.29	Comparison of terminal velocity as a function of the bubble volume for air bubbles rising in 15 mm square capillary filled with 0.1% PAM (PAM1-2) and 0.25% PAM (PAM2-2) solutions.....	66
4.30	Comparison of steady dimensionless velocity of air bubbles as a function of the bubble size for air bubbles rising in 15 mm capillary filled with 0.1% PAM (PAM1-2) and 0.25% PAM (PAM2-2) solutions.....	66
4.31	Steady shapes for air bubbles as a function of the dimensionless bubble size for air bubbles rising in 95% glycerol-water solution (GW3-2) and 95% glycerol-water solution with 10 ppm Triton X-100 (TX1-2) in 15 mm square capillary.....	68
4.32	The (a) length and (b) width of bubbles as a function of bubble size for bubbles in GW3-2, TX1-2, and TX3-2 systems in 15 mm square capillary.....	69

4.33	The length of the bubble as a function of the bubble width for bubbles in GW3-2, TX1-2, and TX3-2 systems in 15 mm square capillary.....	70
4.34	The deformation parameter as a function of the dimensionless bubble size for bubbles in GW3-2, TX1-2, and TX3-2 systems in 15 mm square capillary.....	70
4.35	Comparison of the dimensionless film thickness as a function of the bubble size for bubbles in GW3-2, TX1-2, and TX3-2 systems in 15 mm square capillary.....	71
4.36	Comparison of terminal velocity as a function of the bubble volume for air bubbles in GW3-2, TX1-2, and TX3-2 systems.....	72
4.37	Comparison of steady dimensionless velocity of air bubbles as a function of the bubble size for GW3-2, TX1-2, and TX3-2 systems.....	73

ABSTRACT

AN EXPERIMENTAL STUDY ON THE BUOYANCY-DRIVEN MOTION OF AIR BUBBLES IN SQUARE CHANNELS

by

Vinod Bulusu

University of New Hampshire, September, 2006

The motion of drops and bubbles in confined domains is encountered in several applications such as oil recovery, solvent extraction, paper-making, and microfluidics, among others. In this thesis, the motion of air bubbles in square capillaries moving under the influence of gravity is studied at finite Reynolds numbers. The steady shapes, deformations, film thickness, and velocities of the bubbles as a function of the bubble size are determined experimentally. The bulk fluid phase is either Newtonian, viscoelastic, or a surfactant solution. Bubbles rising in a Newtonian fluid are nearly spherical at lower bubble volumes and become prolate losing their fore and aft symmetry at larger bubble volumes. At lower bulk viscosities, a reentrant cavity develops at the rear of bubble. The critical viscosity at which this shape transition occurs depends on the size of the capillary. The terminal velocity of bubbles increases with volume for small bubble volumes. Even at small bubble volumes, the terminal velocity of the bubbles is much less than the Hadamard-Rybczynski velocity of a spherical bubble with the same

volume. This is due to the effect of the confining walls. As the bubble size becomes comparable to the capillary size, the increased wall drag reduces the velocity of the bubbles and it eventually reaches a plateau value, which is independent of the bubble size. In the presence of elastic effects, the rising bubbles show an axisymmetric pointed cusp at the trailing edge. The steady bubble velocities in viscoelastic fluids are much higher than the Hadamard-Rybczynski velocity for an equivalent bubble moving in a quiescent Newtonian fluid with the same zero shear viscosity. This enhancement in velocity is due to the shear-thinning effect of viscoelastic fluids. In the presence of very small amounts of surfactants, the bubble shapes are more prolate with higher film thicknesses consistent with earlier investigations in cylindrical capillaries. Furthermore, the motion of the bubbles is retarded due to Marangoni effects. As the surfactant concentration is increased, the surfactant adsorption to the interface increases remobilizing the interface.

CHAPTER I

INTRODUCTION

Several industrial applications and natural phenomena involve the flow of drops and bubbles in confined spaces. Examples of such applications are underground transport of pollutants, intrusion of water into oil-bearing strata, solvent extraction processes, and penetration of air into water-saturated networks of fibers in papermaking. During mass transfer processes in gas-liquid systems, the gas is frequently dispersed by means of sieve plate or a perforated plate. The motion of a drop through capillaries also serves as a pore scale model for studying the dynamics of two phase flows through porous media. Several studies have been conducted to characterize the deformation and speed of drops and bubbles in cylindrical capillaries [5,6,17,21].

Microfluidic devices are miniaturized systems which have gained popularity in the recent years since they can be used to perform chemical analysis with very small quantities of reagents. Several applications of two-phase flows in microdevices have been identified such as using microscale droplets as drug-delivery vehicles, actuators, microreactors, and microbubble analysis in DNA solutions [8]. In microfluidic devices, the capillaries are either square or rectangular in cross-section due to fabrication limitations. The dynamics

of drops in a rectangular channel differ from that in a cylindrical capillary due to the non-uniform fluid film surrounding the drop. There are very few studies of drop dynamics in square or rectangular channels at either the microscale or macroscale. A study of particle motion in a rectangular channel at a macroscale can provide insight into two phase flows in microfluidics.

At a fluid-fluid interface, the fluid properties are constant in the bulk of the two fluids and change very rapidly but continuously in the interfacial region. However, due to lack of appropriate molecular theories, the interface is modeled as a massless macroscopic surface where the fluid properties are maintained at their bulk values on either side of the interface and change discontinuously at the interface. Furthermore, the fluid interface is characterized by an interfacial tension, σ , which may depend on the temperature, pressure, concentration of any impurities, or charges in the system. Physically, the interfacial tension is interpreted as the net inward force of molecular attraction per unit length experienced by a fluid that minimizes its surface area or the work done in generating a unit area of the fluid interface. Since the interface is a massless surface with zero volume, the net force acting on the interface must be zero. A force balance at the interface can be written as,

$$(p_{d,tot} - p_{tot})\mathbf{n} + (\boldsymbol{\tau} - \boldsymbol{\tau}_d) \cdot \mathbf{n} + \nabla\sigma - \sigma(\nabla \cdot \mathbf{n})\mathbf{n} = 0 \quad (1.1)$$

where quantities with the subscript d represent the drop phase, p_{tot} and $\boldsymbol{\tau}$ represent the actual total pressure and the deviatoric stress tensor in the fluids, and \mathbf{n} represents the

outward pointing unit normal. Equation (1.1) shows that the total stress undergoes a jump as the interface is crossed. The normal stress jumps by an amount $\sigma(\nabla \cdot \mathbf{n})$, that is, interfacial tension multiplied by the curvature of the interface. The tangential stress, on the other hand, jumps by an amount $\nabla \sigma$, that is, the gradient in the interfacial tension along the interface. Equation (1.1) is applied at the fluid-fluid interface to determine the dynamics of drops and bubbles in confined domains. However, the location of the interface is not known *a priori* and is dependent on the state of stress in the fluid, the interfacial tension, and the variation of interfacial tension at the interface.

Newtonian Systems

In several of the above applications, a drop or bubble is suspended in a Newtonian liquid such as water, glycerol, or silicone oil. For a Newtonian fluid the shear stress is linearly proportional to the velocity gradient in the direction perpendicular to the plane of shear. The constant of proportionality is the viscosity of the fluid. The viscosity of a single component Newtonian fluid depends only on temperature and pressure of the fluid. The viscosity of a Newtonian fluid mixture depends on the chemical composition of the fluid mixture.

For the buoyancy-driven motion of a spherical bubble through a quiescent Newtonian fluid, the governing equations can be solved to give the Hadamard-Rybczynski solution for the translation velocity of the bubble,

$$U_{HR} = \frac{a^2 g (\rho - \rho_d)}{3\mu} \quad (1.2)$$

where a is the radius of the spherical bubble, ρ and ρ_d are the densities of the bulk fluid and the drop fluid respectively, and μ is the viscosity of the bulk fluid.

Viscoelastic Systems

A number of applications in the polymer, food, and pharmaceutical industries involve fluids such as polymer melts, mayonnaise, shampoo and so on. Such fluids have both viscous and elastic properties. To enhance the properties of polymers used in the paint and coating industry, the polymers are often blended with other polymers. This is an inexpensive way of improving the properties of polymers. However, the mechanical mixing of two immiscible polymers results in an emulsion with one polymer suspended as droplets in the other polymer. Therefore, a better understanding of two-phase flows in viscoelastic fluids is important.

Viscoelastic fluids have mechanical properties intermediate between ordinary liquids and ordinary solids. Ordinary liquids attain the shape of a container while ordinary solids maintain their shape indefinitely. Viscoelastic fluids, in contrast, maintain their shape for a certain time but eventually flow. They also retain the memory of their previous configuration, that is, once the stress is removed the fluid tends to go back to its initial stress-free position. This behavior is attributed to the large molecules that viscoelastic

fluids are made of. When the molecules are stretched and aligned along the path of fluid motion, an extra tension is induced. The additional normal stress induced in viscoelastic fluids leads to dynamics which are not seen in Newtonian fluids. One such phenomenon is that of rod-climbing. A rotating rod inserted in a beaker filled with a Newtonian fluid generates a vortex which dips below the level of the fluid (see Figure 1.1(a)). If the beaker is filled with a viscoelastic fluid, it climbs up the rod due to normal forces generated in the fluid (see Figure 1.1(b)). At comparable speeds, the response of a viscoelastic fluid is dramatic as compared to the Newtonian fluid. Die-swelling is a phenomenon that is also observed in viscoelastic fluids. The diameter of a free jet of Newtonian fluid shows a small increase of about 13% for smaller Reynolds number and reduces by about 13% for larger Reynolds numbers (see Figure 1.2(a)). The diameter of a free jet of viscoelastic fluid, on the other hand, shows an increase of about 300% [4].

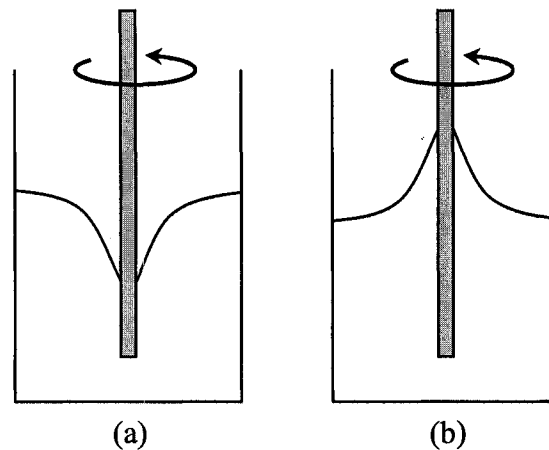


Figure 1.1: Rod-climbing phenomena observed in a viscoelastic fluid when a rod is rotated in a beaker filled with (a) Newtonian fluid and (b) viscoelastic fluid.

The dynamics of two-phase viscoelastic fluids is significantly different from dynamics of two-phase Newtonian fluids. The extension of polymer molecules at the rear stagnation point of a bubble rising in a viscoelastic fluid leads to large normal stresses. As a result, the bubble shows increased deformations at the rear stagnation point and cusped shapes

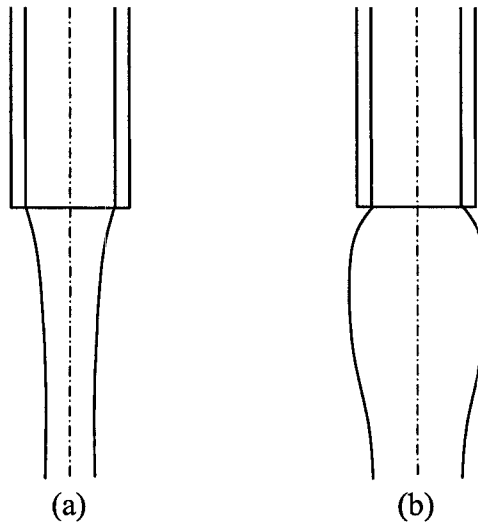


Figure 1.2: Die-swelling phenomena observed in a viscoelastic fluid as a free jet of (a) Newtonian fluid and (b) viscoelastic fluid flows out of a capillary tube.

are formed if the surface tension is not strong enough. Bubbles rising in a cylindrical capillary filled with a viscoelastic fluid show two-dimensional cusp shapes that have not been observed in Newtonian fluids [16]. The cusps are pointed in one direction and flattened in the perpendicular direction (see Figure 1.3). Some studies show a discontinuity in the terminal velocity as the bubble volume is increased beyond a critical volume [3]. It has been suggested that polymer molecules in the viscoelastic fluid act like surfactants to immobilize the interface of small bubbles leading to the velocity jump [1]. The “negative” wake seen behind bubbles is also believed to be responsible for the

cusped shape and velocity discontinuity observed in two-phase viscoelastic fluids [9,11]. The occurrence of cusped shapes and the velocity discontinuity is affected by the presence and cross-section of the confining wall [11,16]. In this study, the effect of elasticity on the dynamics of bubbles rising in a square capillary with bubble sizes comparable to the channel size will be determined.

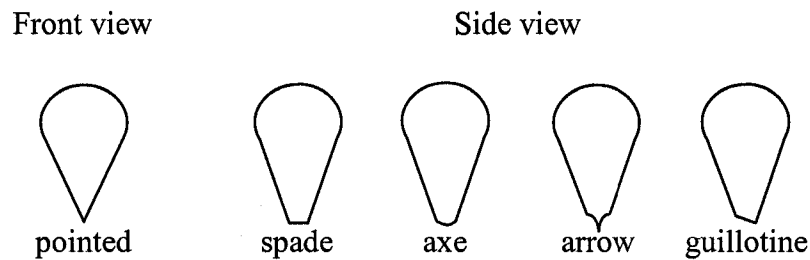


Figure 1.3: Schematic of the two-dimensional cusp shapes observed for motion of air bubbles in a capillary filled with a viscoelastic fluid.

Surfactant Systems

Surfactants are surface-active agents that are either added to two-phase systems as stabilizers, emulsifiers, or may be present as impurities. Surfactants contain a hydrophilic (water-loving) head and a hydrophobic (water-repelling) tail. At a liquid-liquid interface, surfactant molecules align along the interface such that the hydrophilic end remains in the water phase while the hydrophobic end stays in the non-aqueous phase. This lowers the energy of the interface resulting in a reduction in surface tension. Surfactant adsorption at the interface of drops and bubbles alters the stress conditions and causes the resulting hydrodynamics to differ significantly from surfactant-free systems.

Surfactants can affect drop/bubble dynamics in several ways. Surfactants get redistributed along the interface due to surface convection and surface diffusion. In addition, the surfactant concentration is affected by area changes resulting from interface deformations. Furthermore, surfactant may be deposited on the interface and depleted from the interface due to an adsorption-desorption mechanism. The relative timescales of surface convection, bulk diffusion, and adsorption-desorption determines the surfactant concentration at the interface. If surfactant transport to the interface is rapid compared to the hydrodynamic timescales (as can occur at elevated bulk concentrations of surfactants with fast adsorption-desorption kinetics), the drop and bubble mechanics are altered only by a lower, uniform surface tension. In contrast, non-equilibrium surface tensions may develop if the rate of surfactant transport to the interface is slow compared to either the timescale for surface convection along the interface, or the timescale for surface dilatation. If the surfactant distribution is non-uniform, there are two mechanical consequences. First, the tangential stress balance is altered by surface tension gradients (see Equation (1.1)) that exert Marangoni stresses. These stresses pull toward regions of elevated surface tension and slow the tangential velocity of the interface. Second, the normal stress jump is also altered; regions of locally reduced surface tension require larger local curvatures to balance normal stresses. Thus, low surface tension regions deform to become more highly curved, leading to shapes which differ strongly from those realized in the absence of surfactant. Therefore, depending on the surfactant mass transfer kinetics, differing hydrodynamic responses of the fluid particle to surfactant addition can be anticipated.

Objectives

The motion of long bubbles in Newtonian fluids in confined domains has been studied extensively in cylindrical tubes and to a limited extent in square channels. However, there are no studies on the motion of bubbles comparable to the tube size in square capillaries. Most previous studies on free surface flows in viscoelastic fluids are restricted to the buoyancy-driven motion of bubbles in a quiescent non-Newtonian fluid. There are a few studies on the buoyancy-driven motion of long bubbles in circular capillaries filled with a viscoelastic fluid. The effect of surfactants on the motion of long bubbles in cylindrical tubes has been studied asymptotically and experimentally. The dynamics of finite drops and bubbles rising in a cylindrical tube in the presence of surfactants has been studied experimentally. We are not aware of any studies on the effects of surfactants or elastic stresses on the motion of finite sized bubbles in square capillaries. The aim of this project is to further our understanding of the motion of bubbles rising under gravity in a square channel for bubble sizes comparable to the channel size. The specific goals of this study are to determine

- the parameters governing the steady shapes and velocities of bubbles rising in a square capillary filled with a Newtonian fluid,
- the effect of bubble volume on the steady velocity of the bubble in the capillary for bubble sizes comparable to the size of the bubble,
- the effect of elasticity of fluid on the deformation and mobility of bubbles, and
- the effect of surfactant concentration in modifying the steady shape and velocity of a bubble rising in a Newtonian liquid.

To achieve these goals, an experimental study is conducted to investigate the motion of bubbles in a vertical square tube in the absence of any applied pressure gradients. The suspending medium is a Newtonian fluid, a surfactant solution, or a polymer solution. The results to date on the motion of bubbles rising in confined geometries are discussed in Chapter II. Chapter III describes the experimental set up and the systems studied in this thesis. Finally, the results of the experimental study are presented in Chapter IV.

CHAPTER II

BACKGROUND

Newtonian Systems

The motion of long bubbles in Newtonian fluids in confined domains has been studied extensively in cylindrical tubes [6, 17, 21]. There are very limited studies on the motion of bubbles comparable to the tube size and drops of finite viscosity [5]. In comparison, the studies in square channels are limited to the motion of long bubbles in Newtonian fluids [7,10,12-14,19,31]. One of the earliest analyses on the motion of a long air bubble in a tube was carried out by Bretherton [6]. Lubrication analysis was used to study two cases of bubble flow in the tube. In the first case, the tube radius was small and the gravitational forces were negligible. In the second case, the buoyancy-driven motion of a bubble in a vertical tube sealed at the bottom end was considered. The fluid was assumed to be perfectly wetting with a constant interfacial tension. For the case of buoyancy-driven motion, axial symmetry was assumed for the bubble which had a front and rear meniscus separated by a region in which a uniform film of fluid was draining under the effect of gravity. At the rear and front menisci viscous stresses were negligible and a

force balance between surface tension and gravitational forces determined the shape of the bubble. Bretherton found that there is no bubble motion in the tube if $Bo_R < 0.842$, where $Bo_R = \rho g R^2 / \sigma$ is the Bond number which gives the ratio of gravitational forces to the interfacial forces. Here, ρ is the difference in density between the fluids outside and inside the bubble, σ is the surface tension, and R is tube radius. For $Bo_R > 0.842$, the rate of rise of the bubbles is given by $Bo_R - 0.842 = 1.25 Ca_R^{2/9} + 2.24 Ca_R^{1/3}$, where $Ca_R = \mu U_d / \sigma$ is the capillary number which gives the ratio of viscous forces to the interfacial forces. Here, μ is the viscosity of the fluid and U_d is the velocity of the bubble. The film thickness in the central region is proportional to $Ca_R^{2/3}$. The rear meniscus has a wave-like appearance. Bretherton's analysis is limited to vanishing values of Ca_R with about 10% error for $Ca_R = 8 \times 10^{-5}$.

Reinelt [21] solved the flow around a finger rising in a vertical tube in the creeping flow limit for $0.0001 \leq Ca_R \leq 0.1$, much higher than the Ca_R values in Bretherton's study. For a long bubble rising in the vertical tube, the shape of the front and rear of the bubble are independent of the bubble size. The length of the central portion of the bubble increases as the bubble volume increases and the velocity of the bubble is steady. Thus the motion of long bubbles in a vertical tube can be approximated by the motion of finger of air rising due to drainage of liquid from a vertical tube sealed at one end. The problem is governed by only three non-dimensional parameters, the ratio of radius of finger to the tube radius, β , the ratio of viscous force to surface tension force, Ca_R , and the ratio of gravitational force to interfacial tension, Bo_R . The numerical solution for

Bo_R as a function of Ca_R showed that as the Bond number for the system increased, the capillary number for the flow also increased. In the limit of $Ca_R \rightarrow 0$, the numerical solution of Reinelt matched the perturbation solution of Bretherton.

Borhan and Pallinti [5] studied the buoyancy-driven motion of air bubbles and viscous drops in cylindrical channels experimentally where the drops and bubble sizes were comparable to the size of the tube. They considered a wide range of viscosity ratios, density ratios, Bond numbers, Bo_R , and capillary numbers, Ca_R with Reynolds number, $Re_R = \rho UR/\mu$ in the creeping flow regime. The air bubbles rising in the tube were near spherical for small bubble volumes. As the bubble volume increased, the bubbles became elongated ellipsoids while maintaining their fore and aft symmetry. However, this was not the case for viscous drops which were more curved near the front meniscus and flattened at the rear meniscus. The fore and aft symmetry of the viscous drops was restored if the Bond number of the fluid system was increased while keeping all other parameters constant. Even for drops with vanishing viscosity, the authors observed that as the Bond number was increased, the drops were more elongated with increased fore and aft symmetry. The drop deformation was measured in terms of a deformation parameter defined as the ratio of perimeter of the drop to the perimeter of a spherical drop of the same volume. Initially, as the drop size was increased, its radial and axial dimension grew almost linearly. As the drop size increased, the growth in the radial direction reached a limiting value corresponding to a constant film thickness between the cylindrical drop and the capillary wall. As the Bond number was increased for drops with all other parameters held constant, the film thickness increased very rapidly and

reached a limiting value for large values of the Bond number. The film thickness was not a very strong function of the viscosity ratio and agreed with the asymptotic solutions of Bretherton [6] and the numerical solutions of Reinelt [21].

Borhan and Pallinti [5] observed that for small values of the Bond number, the terminal velocities of the drops showed a maxima in velocity for small drop sizes. The maximum in the terminal velocity was a consequence of the retarding effect of the wall drag which increased as the drop size increased. As the drop size increased further the terminal velocity reached a steady value which was independent of the drop size. In the case of higher Bond numbers, the velocity increased monotonically and reached a steady value. The dimensionless drop speed for long drops with similar viscosity ratios showed that the drop speed increased rapidly with increasing Bond number but reached a steady value for large values of the Bond number. The authors also observed that for $Bo_R < 0.87$, no motion of drops was observed for any of the viscosity ratios studied. This limiting value agreed well with the analysis of Bretherton [6].

The effect of non-circular confining walls on the pressure-driven or combined pressure- and buoyancy-driven motion of long bubbles has been studied asymptotically [14,19,32,33], experimentally [12], and numerically [10]. Ratulowski and Chang [19] used an arclength-angle formulation of a composite lubrication approximation to extend the results of Bretherton to higher capillary numbers. They also solved the film thickness and the pressure drop across a bubble translating in a square capillary for capillary numbers greater than 3×10^{-3} . They determined that the bubble shape is axisymmetric

for $Ca > 0.04$. For $Ca < 0.04$, the bubble is non-axisymmetric in the flat film region and is axisymmetric in the front. The pressure-driven motion of long bubbles in polygonal capillaries in the limit of $Ca \rightarrow 0$ was considered by Wong et al. [32, 33]. The authors showed that the major difference in the film profile from the cylindrical profile was that the film thickness in the front contact region in a polygonal capillary changed from $O(Ca^{2/3})$ at the leading edge to $O(Ca)$ along the direction of bubble flow. This difference was attributed to the rearrangement of the film in the downstream section because of surface tension. The liquid film rearranges in two stages. For $x \sim 1/Ca$, the film is rearranged into a parabolic shape. Here x is the dimensionless downstream distance from the front of the bubble. When $x \gg 1/Ca$, the film height reduces as the film fluid leaks through film boundary. For the above studies, the effects of gravity was assumed to be negligible ($Bo \approx 0$).

Kolb and Cerro [12-14] studied the motion of long bubbles in tubes of square cross section with intermediate to high capillary and Bond numbers as a model for describing flow through porous media. Their experimental results [12] showed that the annular film deposited by the bubble was either axis-symmetric or axis-asymmetric depending on the capillary number. For lower capillary numbers ($Ca < 0.1$), the gas bubble flattened against the tube walls and the bubble was seen as axis-asymmetric. At higher capillary numbers ($Ca > 0.1$) an axis-symmetric bubble was found. Also the radius of the bubbles reduced asymptotically at larger capillary numbers. Similar to the Bretherton analysis, the bubble profile was divided into three regions: a cap region, a transition region, and a uniform film region. The cap region was significantly large at lower capillary numbers,

resulting in small free surface inclination angles. With increasing capillary numbers, the cap region reduced and the free-surface inclination angles increased. At a capillary number of about 0.6, the cap region completely disappeared. Also the bubble velocity at lower capillary numbers was higher than the average but less than the maximum liquid velocity ahead of the bubble. The liquid outside the bubble flowed past the bubble into the film while the liquid inside the bubble recirculated. This resulted in a stagnation ring on the bubble interface. The authors found that the stagnation ring moved towards the tip of the bubble with increasing capillary number. Kolb and Cerro [13] derived an analytical expression for the velocity profile between the circular bubble and the square tube walls. The authors also used the lubrication approximation in conjunction with the analytical velocity profile to develop a film evolution equation [14]. The film evolution equation was integrated numerically over a wide range of capillary and Bond numbers and showed that the deposited annular film depended on the size of the capillary, velocity of the bubble, and the physical properties of the fluid.

The effect of large capillary numbers on the dynamics of air bubbles translating in rectangular and elliptical capillaries in the absence of inertial effects ($Re \rightarrow 0$) was considered by Hazel and Heil [10]. They used finite-element methods to solve the free-surface Stokes equation for finite capillary and Bond numbers. The shape of the interface and the pressure drop across the bubble was determined in terms of capillary number. For square capillaries, the authors found that the bubble radius increased with decreasing capillary number. Below a critical capillary number the bubble interface downstream of the tip became axis-asymmetric similar to the observations of Ratulowski and Chang and

Kolb and Cerro. However, they also observed an axis-asymmetry developing immediately behind the finger tip for $Ca > 4$. The leakage flow along the corners of the square tube reduced the pressure in the corners and the air-liquid interface moved radially outwards causing the asymmetry. For a given Ca , a positive Bond number increased the film thickness.

The buoyancy-driven motion of long bubbles in square channels has been studied experimentally by Clanet et al. [7] and numerically by Taha and Cui [31]. Clanet et al. [7] studied the motion of bubbles rising in tubes of arbitrary cross-sections and determined the relation between the rise velocity and the cross-section of the tube. For bubbles at high Reynolds numbers and high Kapitza numbers, $Ka = (\sigma^3 \rho / g \mu^4)^{1/6}$, the dimensional velocity of long bubbles in square tubes was found to be $U_d = 0.54 \sqrt{g R_H}$, where R_H is the hydraulic radius of the tube. For bubbles at low Reynolds and Kapitza numbers and large Bond numbers, the bubble rise velocity was given by $U_d = 0.043 \rho g R_H^2 / \mu$. For all the data presented by Clanet et al. [7], the transition from high- to low- Reynolds number occurred at a critical Reynolds number, $Re_s \equiv U_d (S/P) \rho / \mu \approx 4$, where S and P are the area and perimeter of the tube. Taha and Cui [31] used a volume-of-fluid (VOF) method to study the shape and mobility of slug flows in square capillaries. The authors showed that for low capillary numbers, the bubbles tend to flatten out against the wall losing their axisymmetry. As the capillary number was increased, the rear of the bubble flattens out and eventually develops a negative curvature at the rear stagnation point.

Viscoelastic Systems

Most previous studies of free-surface flows in viscoelastic fluids have been restricted to the buoyancy-driven motion of bubbles in a quiescent non-Newtonian fluid [1,3,9,11,15,16]. There are a limited number of studies on the buoyancy-driven motion of long bubbles in circular capillaries filled with a viscoelastic fluid [26-28]. The behavior of bubbles in non-Newtonian fluids shows several phenomena such as cusp-formation, velocity discontinuity, and negative-wake formation that have not been observed for Newtonian fluid flows. Surfactants may be deliberately added to these systems to modify the critical conditions under which the jump discontinuity is observed [22-25].

One of the earliest studies on the motion of air bubbles rising under gravity in quiescent non-Newtonian fluids was attempted by Astarita and Apuzzo [3]. For elastic fluids, they observed that the bubbles with lower volume were prolate with a distinct cusp at the rear stagnation point. As the bubble volume was increased, the bubbles looked like spherical caps still maintaining the cusps at the rear. The steady migration velocity of the bubbles increased as the bubble volume increased. For bubbles rising in an elastic fluid, at a critical bubble volume, the bubble velocity increased abruptly by a factor which was as large as 6 for some fluid systems. The authors proposed that the jump in velocity at a critical bubble volume in the presence of elasticity was the result of a change in the

interfacial boundary condition from a “no-slip” condition to a “free-shear” condition. To validate the hypothesis put forth by Astarita and Apuzzo, Leal et al. [15] conducted an experimental study on the rise of air bubbles and falling of glass spheres in a Separan-AP30 solution of varying concentrations. They found that the air bubbles rising in the elastic solution did show a jump in the terminal velocity while the glass spheres showed no jump in the terminal velocity. This provided strong evidence to the hypothesis that the velocity discontinuity is the effect of a transition of the interfacial condition from the Stokes to the Hadamard regime.

Hassager [9] used Laser-Doppler anemometry to measure the liquid velocity in the wake behind a bubble rising in a non-Newtonian liquid. Whereas the fluid in the wake behind a bubble rising in a Newtonian fluid flows towards the bubble, the velocity of the fluid behind the bubbles in case of an elastic liquid was away from the direction of rising bubbles. Hassager termed this phenomenon as “negative wake”. Furthermore, photographs of large bubbles ($> 50 \text{ mm}^3$) taken at mutually perpendicular directions revealed a two-dimensional cusp shape at the rear pole. In one view, the bubble showed a pointed cusp at the rear pole while in the perpendicular view, the bubble showed a knife-edge. The experiments were carried out in a glass cylinder and the observed two-dimensional cusps were unexpected and attributed to the elasticity of the fluid.

Liu et al. [16] conducted experiments on the rise of bubbles in a variety of columns with cross-sections such as circular, square, and rectangular with different aspect ratios. Bubbles with very small volume were spherical in shape. When the bubble volume was

increased, the bubble shape changed from spherical to prolate. Further increase in the volume of the bubble led to the formation of a two-dimensional cusp at the rear of the bubble accompanied by a jump in its terminal velocity. The bubble volumes at which the transitions in shape occurred depended on the bulk fluid properties. The two-dimensional cusps observed by Liu et al. were pointed in one orientation and broad in the perpendicular orientation. The broad edge took on several forms such as an axe edge, and arrow edge, flat spade edge similar to Hassager [9], as well as a guillotine edge. The development of the two-dimensional cusp depended on the properties of the bulk fluid but was independent of the cross-section of the column. In case of rectangular columns there were three stable orientations but there was no preferred orientation when the column cross-section is circular or the sidewalls are far away from the rising bubble.

Herrera-Velarde et al. [11] used particle-image-velocimetry (PIV) techniques to study the flow field around a bubble rising in a viscoelastic fluid near the critical bubble volume. They conducted experiments in square columns of varying cross-sectional areas filled with polyacrylamide (PAM) solutions of varying concentrations. They observed that the terminal velocity of air bubbles and the critical bubble volume reduced with increasing PAM concentration. Experiments on the same air-fluid system in columns of varying sizes showed that as the column size was reduced, the terminal velocity of the bubbles also reduced. The magnitude of the jump discontinuity reduced as the wall effects became significant though the critical volume at which the jump discontinuity occurred remained unchanged. The PIV data showed that the wake behind the rising bubble below the critical bubble volume was not “negative” but “negative” wake was

observed for bubbles beyond the critical bubble volume. However, they did not observe any significant change in shape below and above the critical bubble volume. Though the “negative” wake is associated with the discontinuity in the terminal velocity observed for bubbles rising in a viscoelastic fluid, the authors could not ascertain what caused the “negative” wake.

Acharya et al. [1] suggested that the polymer molecules in viscoelastic fluids acted as surfactants molecules, adsorbed at the air-fluid interface, and were responsible for the change in the boundary condition from a rigid surface to a free surface. Rodrigue and co-authors [22-25] also studied the effect of surfactants on the bubble shape and dynamics of bubbles rising in a viscoelastic fluid. They have shown that surfactants can alter the conditions for the onset of terminal velocity discontinuity for the rise of bubbles in a viscoelastic fluid. Addition of small amounts of surfactants can induce a discontinuity in terminal velocity in a viscoelastic solution which exhibits a continuous velocity-volume relationship in the absence of surfactants. At surfactant concentrations above the critical association concentration (CAC), the discontinuity in the velocity-volume relationship disappears as a consequence of the remobilization of the interface. Similarly, the discontinuity in velocity was seen when the elasticity of the fluid was increased by increasing the concentration of the polymer solution. Rodrigue et al. [25] identified a 'modified' capillary number, $\alpha = Ca De / Ma$, where Ca is the capillary number, De is the Deborah number, and Ma is the Marangoni number, such that for small values of α the velocity is continuous with bubble volume and a discontinuity is observed when $\alpha > 1$.

There are very limited studies on the motion of bubbles in confined domains filled with viscoelastic fluids and are restricted to cylindrical capillaries. Recently, Sousa and co-workers [26-28] have used simultaneous PIV and shadowgraphy techniques to study the shape and flow fields around a long bubble (Taylor bubbles) rising in cylindrical tubes filled with non-Newtonian fluids. They conducted experiments with carboxymethyl cellulose solutions and polyacrylamide (PAM) solutions of varying concentrations. The shape of Taylor bubbles was prolate spheroid at the leading edge with higher curvatures for higher viscosity fluids. The bubble radius increased and reached a maximum value at a certain distance from the nose of the bubble. For higher concentrations of carboxymethyl cellulose solutions (> 0.8 wt %) which exhibit viscoelastic fluid behavior, the bubbles show a two-dimensional cusp at the rear of the bubble and a “negative” wake. In case of PAM solutions, the authors found that flow field behind the bubbles was not always axisymmetric and showed a “negative” wake at higher concentrations.

Surfactant Systems

The effect of surfactant concentration on the bubble motion in cylindrical tubes has been studied for long bubbles asymptotically and experimentally [18,20,29,30]. The effect of varying the surfactant concentration on the bubble shape and velocity has been reported. Furthermore, surfactant transport involving the adsorption and diffusion of surfactant at the surface has also been investigated [29,30]. The dynamics of finite drops and bubbles rising in a cylindrical tube in the presence of surfactants has been studied experimentally

[2]. We are not aware of any studies on the effect of surfactants on the motion of bubbles in square capillaries.

The lubrication approximation by Bretherton [6] underpredicts the film thickness observed experimentally at small capillary numbers and this discrepancy is attributed to the presence of small amounts of impurities in the experiments. Ratulowski and Chang [20] conducted an asymptotic analysis to study the effect of surfactants on the shape and mobility of long bubbles translating in a cylindrical tube for different regimes of surfactant transport conditions. If the surfactant transport to the interface is slow as compared to convection, gradients of surfactant develop along the interface resulting in an increase in the film thickness by a maximum factor of $4^{2/3}$ over that of Bretherton's result. Park [18] studied the effect of surfactants on the motion of finite-sized bubbles in a cylindrical capillary in the limit of small capillary numbers. He showed that film thickening in the presence of surfactants is observed only if the bubble is longer than a critical bubble length. Stebe et al. [29,30] experimentally and theoretically studied the effect of surfactants on the motion of long bubbles in capillaries for various regimes of surfactant transport. The authors showed that for a surfactant laden interface, when no barrier exists on bulk diffusion, the interface behaves as a clean interface. However, the interface becomes more easily deformable at the higher concentration of surfactants as the surface tension is lower.

Almatroushi and Borhan [2] experimentally studied the effect of surfactants on the buoyancy-driven motion of drops and bubbles in a cylindrical tube at low Reynolds

numbers ($Re < 0.1$). In the absence of surfactants, the terminal velocity of the bubbles and drops increased at first with increasing drop size, but reduced with increasing drop size due to increasing wall effects and finally reached a plateau value. In the presence of surfactants below critical micelle concentration (CMC), it was observed that the location of maximum terminal velocity and the occurrence of plateau occurred at a higher drop size as the surfactant concentration was increased. Furthermore, the magnitude of the maximum terminal velocity was reduced as the surfactant concentration was increased. For surfactant concentrations below CMC, the bubbles were retarded due to Marangoni effects. For surfactant concentrations beyond the CMC, the mobility of smaller bubbles remained unaffected while the mobility of larger bubbles was increased slightly. The shape of small bubbles was independent of surfactant concentration, but for larger bubbles the deformation increased with increasing surfactant concentration. For a bubble of a given size it was seen that the radial length was lower and the axial length was higher in the presence of surfactants.

CHAPTER III

EXPERIMENTAL METHODS

Experimental Setup

The experimental setup used for studying the dynamics of bubbles in square channels is shown in Figure 3.1. Acrylic tubes of square cross-section with both ends open were used. The bottom ends of the tubes were sealed with removable acrylic ends fitted with a rubber septum to serve as an injection port. Three tubes of sizes 10 mm × 10 mm, 15 mm × 15 mm, and 20 mm × 20 mm were used in the experiments. Each tube had a length which was at least 30 times the hydraulic diameter of the tube. The tube was clamped to a vertical stand and a level set was used to ensure that the tube was perpendicular to the ground. This allowed the bubbles to remain along the central axis of the tube as they translated through the tube.

The vertical tube was placed in front of a CCD camera to capture images of the translating bubbles. A Pulnix TM-1325 CL camera with a speed of 30 frames per second at a resolution of 1392 × 1040 was used in the experiments. The camera was connected via a cameralink to a National Instruments (NI-1428) frame grabber board fitted to a

personal computer. The measurement and automation software and Labview software loaded on the personal computer (PC) was used to control the camera and capture images. A fiberglass light source was used to provide uniform back-illumination to capture images of the bubbles.

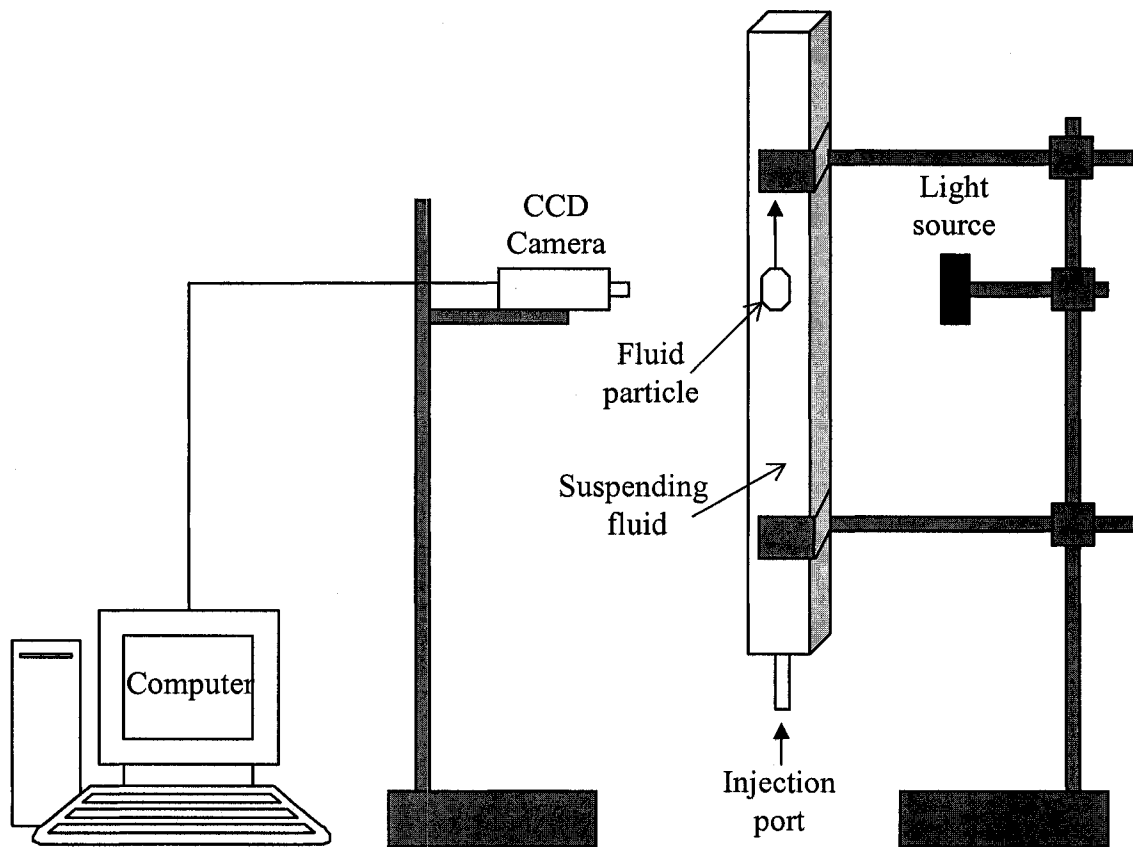


Figure 3.1: Schematic of the experimental setup used to study the buoyancy-driven motion of bubbles in square channel.

Experimental Procedure

The liquid to be tested was placed in a vacuum degasser to remove any air bubbles from the fluid. The tube was filled with the test fluid making sure that bubble formation was minimized. The presence of small air bubbles in the tube interferes with the motion of single bubbles being studied. After filling the tube with the test fluid, the tube was clamped to a stand and leveled. The camera was placed on a leveled tripod far enough from the injection port so as to capture the steady shape and velocity of the bubbles. This was established by measuring the bubble velocity at two locations far from the injection port and making sure that they were the same.

Using the NI measurement and automation software, appropriate settings for the camera, position of the camera, and the light source were determined. A calibration grid and the CALIBRATE IMAGE routine in the Vision Assistant software were used to generate a calibration image. The calibration image was used to determine the bubble dimensions in microns. After calibrating, the frames per second at which the images were captured was determined by running the GRAB AND SAVE TO AVI routine in Labview 7.1 for a specific time and finding the total frames captured from Vision Assistant software.

After the system is set up, a needle was pierced through the septum and a specific volume of air was injected into the tube. Using the GRAB AND SAVE TO AVI routine in Labview 7.1 the motion of the bubble was recorded as the bubble passed in front of the camera. The image file was then read frame-by-frame using the Vision Assistant

software. The steady velocity of the bubble was calculated by evaluating the displacement of the top of bubble between consecutive frames at known frame rate. The co-ordinates of the edge of the drop were determined by using the EDGE DETECTION routine along with the calibration image. The edge data was input into a C-program (see Appendix A) to calculate the volume of the bubble. The C-program assumes the bubble to be axisymmetric and calculates the volume of bubble as the volume obtained by rotating the projection of the bubble around the vertical axis. The velocity-volume data for any suspending fluid was thus generated.

Since viscoelastic fluids show partial recovery, the fluid must be allowed to relax for a certain amount of time, referred to as the delay time, before the next bubble can be introduced into the system. To determine the delay time required for a given suspending fluid, velocity-volume curves were generated for delay times of 5, 10, 15, and 20 minutes. The required delay time for a given test fluid was established as the minimum delay time for which no change in the velocity-volume curve was observed if the delay time was increased beyond this value. For all the test fluids considered, a delay time of 20 minutes was found to be sufficient and was used for the data presented in this thesis.

Materials and Methods

For our experiment, the Newtonian bulk phase consisted of solutions of glycerol (Aldrich) in water at varying concentrations. The viscoelastic phase was prepared by mixing polyacrylamide (SNF) powder in water or 50% glycerol-water solutions. The

drop phase consisted of air bubbles. The surfactant solutions were prepared by adding Triton X-100 (Alfa Aesar) at ppm levels in 95% glycerol-water solution. Since adding such small amounts of Triton X-100 was difficult, a highly concentrated solution of 20000 ppm Triton X-100 in 95% glycerol-water solution was made. The concentrated solution was diluted with 95% glycerol-water solution to obtain smaller concentrations of Triton X-100. The physical properties of the various chemical compounds used in the experiments are shown in Table 3.1. All solutions were made in percentage by weight basis. The volume of solution needed to fill the tube was determined. The required amount of the reagent, polyacrylamide (PAM) or glycerol was weighed and added to the measured amount of distilled water. After adding the reagent, the solution was stirred in a closed vessel until it was uniform.

Table 3.1: Properties of the chemicals used in the experiment.

Fluids / Materials	Properties
Suspending Phase	
Glycerol	Chemical Formula: $C_3H_8O_3$ Molecular Weight = 92 $\rho = 1260 \text{ kg/m}^3$ $\eta^\circ = 1.5 \text{ kg.m/s}$
Polyacrylamide (PAM)	Chemical Formula: $(CH_2CHCONH_2)_n$ Average Molecular Weight = 1.2-1.4 million Physical State: White solid $\rho = 800 \text{ kg/m}^3$
Drop Phase	
Air	$\rho = 1.2 \text{ kg/m}^3$ $\eta^\circ = 1.8 \times 10^{-5} \text{ kg.m/s}$
Surfactant	
Triton X-100	Chemical Formula: $C_{14}H_{22}O(C_2H_4O)_n$ Average Molecular Weight = 647 Physical State: White solid $\rho = 1060 \text{ kg/m}^3$

The physical properties of the prepared solutions were determined at the same temperature at which the experiments were conducted. The rheological properties of all the test fluids were determined by using a Brookfield cone and plate (LVDV-III+) rheometer. The rheometer was operated with different spindle numbers of CPE51 and CPE52. Rheocalc software was used to control the rheometer and analyze the obtained data. The BEAVIS routine was used to determine the viscosity of the fluid at different shear rates. This was done by incrementing the shear rates by a certain amount (10 s^{-1} for the Newtonian fluids) and waiting for a specific period of time (30 seconds for the Newtonian fluids) so that steady viscosity was attained for the specific shear rate.

In these experiments, three viscoelastic fluid solutions were used: 0.1% PAM solution in water, 0.25% PAM solution in water, and 0.1% PAM solution in 50% glycerol-water solution. The rheological behavior of the viscoelastic PAM solutions was determined at Malvern Instruments, Southborough, MA using a Bohlin C-VOR digital rheometer with a cone and plate geometry. The experiments were conducted at 25°C with shear rates varying from $0.05 - 1000 \text{ s}^{-1}$ with a 10 second delay. The following rheological data was obtained for the viscoelastic fluids:

1. Steady-state shear viscosity

A shearing flow is imposed for a suitable time so that a steady shearing flow is attained. The shear rate in a cone and plate geometry is given by, $\dot{\gamma} = \frac{\Omega}{\tan \alpha}$, where Ω is the steady angular rotation of the cone or plate, and α is the cone angle. The steady shear stress, τ is measured as the force that a liquid exerts on the surface per

unit area of that surface and the steady-state viscosity is determined as, $\eta = \frac{\tau}{\dot{\gamma}}$.

Figure 3.2 shows the steady shear viscosity as a function of shear rate for 0.1% PAM in water, 0.25% PAM in water, and 0.1% PAM in 50% glycerol-water solutions. The low shear rate plateau is known as the zero shear viscosity and is designated as η^0 . The zero shear viscosity is found to be 1.65 Pa.s, 11.83 Pa.s, and 9.78 Pa.s for 0.1% PAM in water, 0.25% PAM in water, and 0.1% PAM in 50% glycerol-water solutions, respectively. The fluid is shear thinning as the steady shear viscosity decreases with increasing shear rate. At higher shear rates the viscosity decreases resembling the solid like fluids.

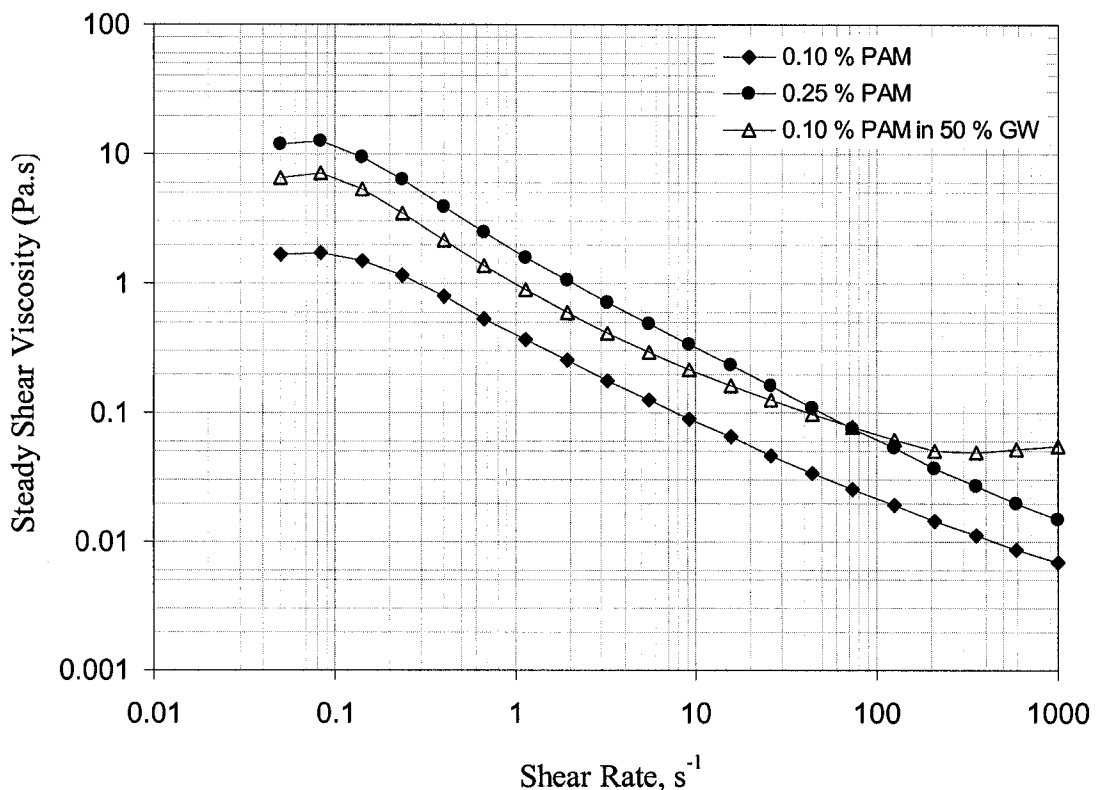


Figure 3.2: Steady shear viscosity as a function of the shear rate for the viscoelastic fluids used in the experiments.

2. **Storage (G') and Loss (G'') Moduli:** In a complex fluid the rate of structural rearrangement can be determined by imposing small amplitude oscillatory shearing. In a cone and plate geometry this kind of motion is achieved by rotating the cone with an angular velocity, $\Omega(t) = \Omega_o \cos(\omega t)$. The shear rate is also a function of time and it is given by $\dot{\gamma}(t) = \Omega(t) / \tan \alpha$ and hence the shear strain, given as the time integral of shear rate, is given by $\gamma = \left(\Omega_o / \omega \right) \sin(\omega t) / \tan \alpha$. The number Ω_o / ω is defined as the amplitude of angular deflection and $\gamma_o = \Omega_o / \omega \tan \alpha$ is defined as the strain amplitude. If γ_o is very small then the fluid is not disturbed by the oscillations and the stress is controlled by the rearrangement of the fluid. The shear stress is the response and it can be split into “in phase” and “out of phase” with the input deformation. The storage modulus (G') can be determined from the “in phase” component of the response and viscous modulus (G'') can be determined from the “out of phase” component of the response. For liquid-like fluids the storage modulus, G' is much less than the loss-modulus, G'' (i.e. $G' \ll G''$) and $G' \propto \omega$ and $G'' \propto \omega^2$. Figures 3.3, 3.4, and 3.5 show the storage and loss moduli as a function of shear strain at a frequency of 1 Hz for 0.1% PAM in water, 0.25% PAM in water, and 0.1% PAM in 50% glycerol-water solutions, respectively. The storage and loss moduli for the three fluids are of the same order of magnitude exhibiting elasticity. The moduli are independent of the shear strain for the range of shear strains considered.

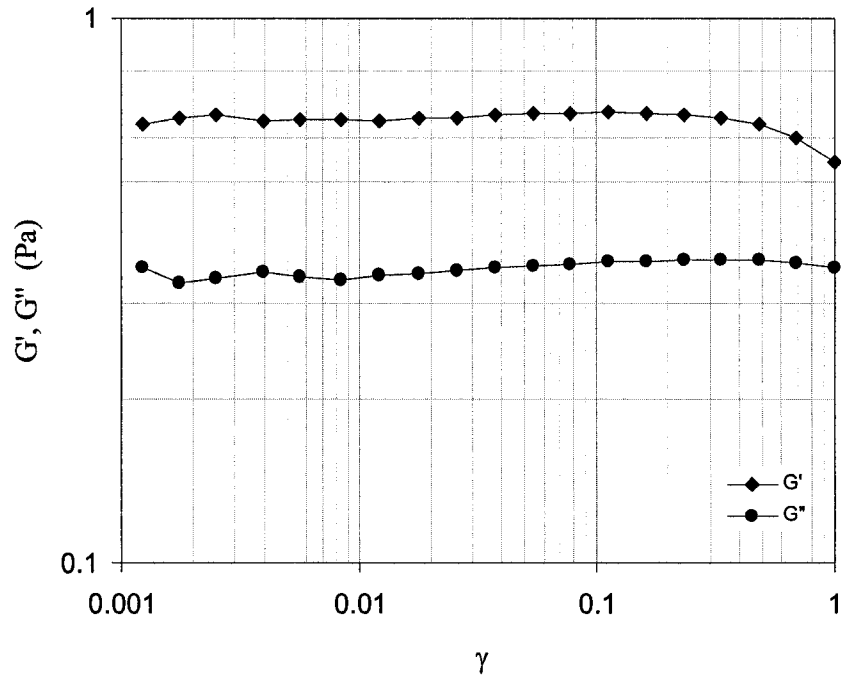


Figure 3.3: Storage modulus (G') and loss modulus (G'') as a function of the shear strain for 0.1 % PAM solution in water.

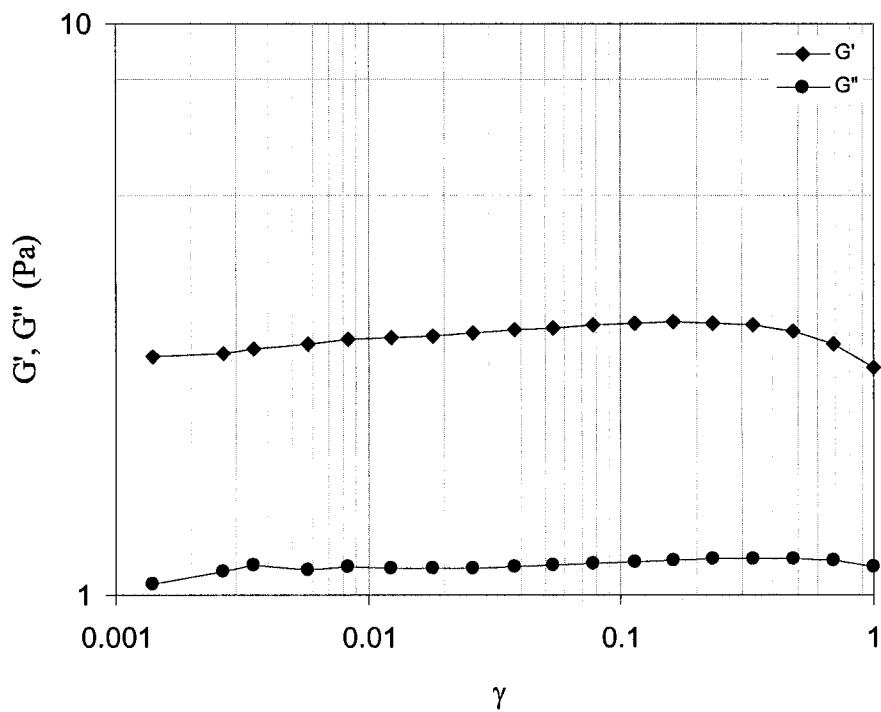


Figure 3.4: Storage modulus (G') and loss modulus (G'') as a function of the shear strain for 0.25 % PAM solution in water.

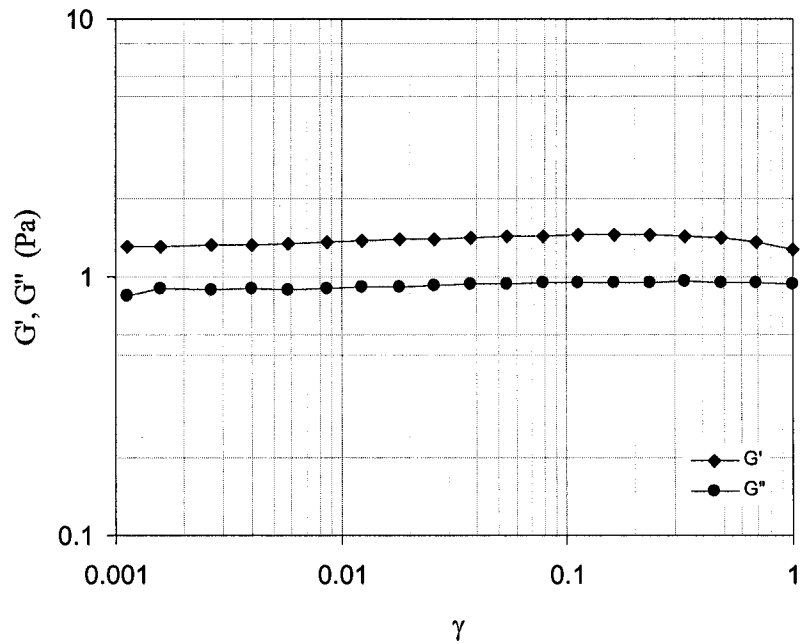


Figure 3.5: Storage modulus (G') and loss modulus (G'') as a function of the shear strain for 0.1 % PAM solution in 50 % glycerol-water solution.

Interfacial tension was determined by Du-Nuoy ring method using Fisher's Model 21 tensiometer. As Triton X-100 is added to the Newtonian fluid, 95% glycerol-water solution, surfactant molecules adsorb at the air-liquid interface, reducing the free energy of the interface, lowering the equilibrium surface tension. The equilibrium surface tension, σ_{eq} as a function of the Triton X-100 concentration is shown in Figure 3.6. The equilibrium surface tension remains unaffected by the addition of 10 ppm of Triton X-100 in 95% glycerol-water solution. As the concentration of Triton X-100 increases, the equilibrium surface tension reduces till a concentration of 10000 ppm. For this study, three surfactant solutions with 10 ppm, 100 ppm, 1000 ppm Triton X-100 in 95% glycerol-water solution were chosen.

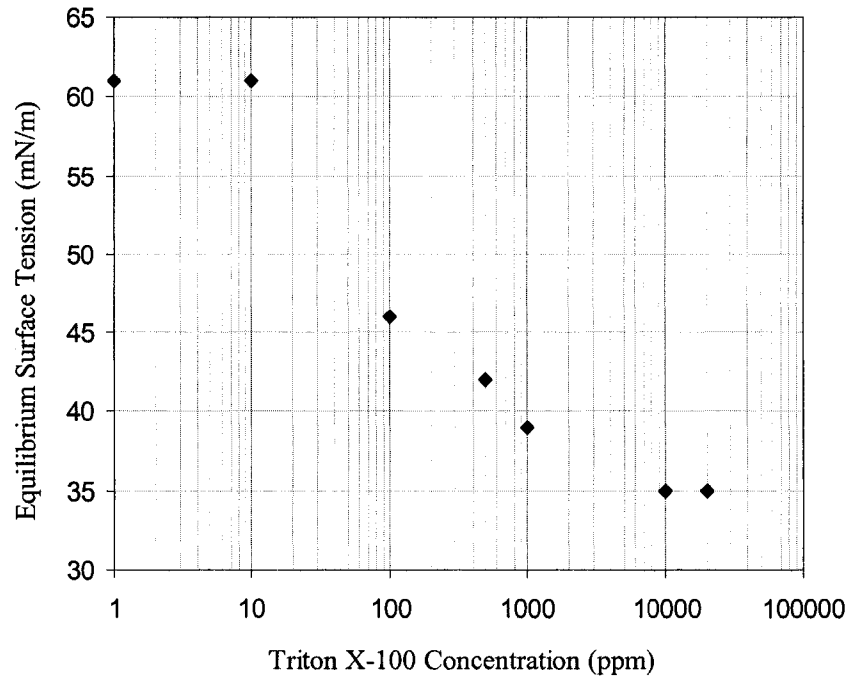


Figure 3.6: Equilibrium surface tension as a function of Triton X-100 concentration in 95% glycerol-water solution.

Material Properties

The schematic of the viscous bubble rising in a vertical tube is shown in Figure 3.7. The density and viscosity of the bulk phase is represented as ρ and η^o , respectively, and the density and viscosity of the drop phase is represented as ρ_d and η_d^o , respectively. The bubble moves with a steady velocity U_d along the axis. The equilibrium interfacial tension between the bulk phase and the drop phase is represented by σ_{eq} . The square channel has a width of h and the bubble size is characterized by the radius, a , of a spherical bubble of the same volume. Therefore,

$$a = \left(\frac{3V_d}{4\pi} \right)^{1/3} \quad (3.1)$$

where V_d is the volume of the bubble. In the cross-sectional view, the bubble may be axisymmetric as seen in Figure 3.7(a) or non-axisymmetric as seen in Figure 3.7(b). In this study, we have assumed that the bubble shape in the cross-section is axisymmetric. The physical properties of the various suspending fluids and bulk fluids used in the experiments are shown in Tables 3.2, 3.3 and 3.4. The hydraulic radius, $R_H=h/2$ of the channel is chosen as the characteristic length scale and the dimensionless drop size is defined as,

$$\kappa = \frac{a}{R_H} \quad (3.2)$$

The bubble velocity, U_d is chosen as the characteristic velocity scale to non-dimensionalize the system and the resulting dimensionless parameters are defined as,

Density ratio,
$$\chi = \frac{\rho_d}{\rho} \quad (3.3)$$

Viscosity ratio,
$$\lambda = \frac{\eta_d^o}{\eta^o} \quad (3.4)$$

Reynolds number,
$$\text{Re} = \frac{R_H U_d \rho}{\eta^o} \quad (3.5)$$

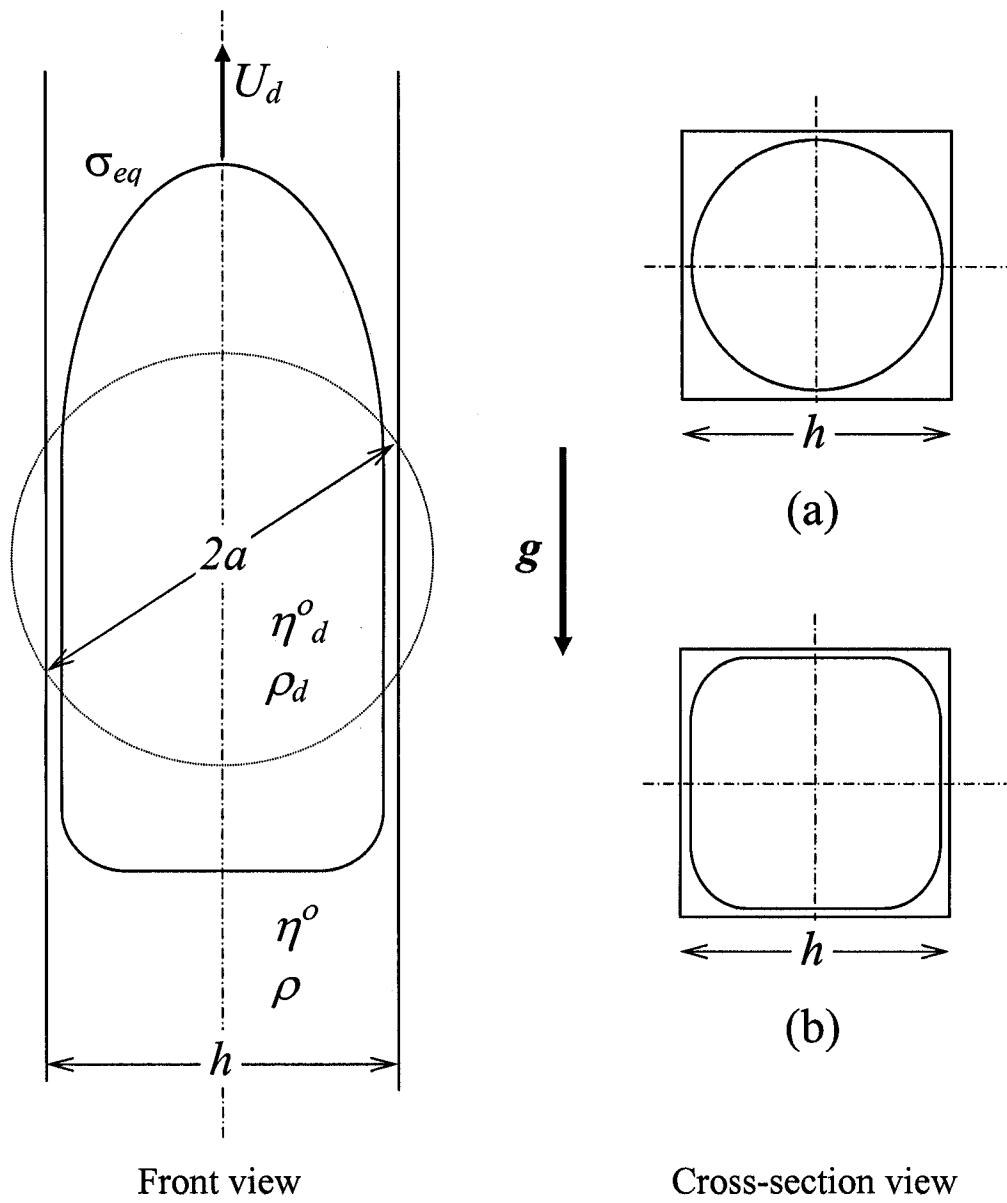


Figure 3.7: Schematic of front view and cross-section view of a bubble rising in a square channel. The bubble may be (a) axisymmetric or (b) non-axisymmetric in the cross-section view.

Bond number,
$$Bo = \frac{(\rho - \rho_d)gR_H^2}{\sigma_{eq}} \quad (3.6)$$

Capillary number,
$$Ca = \frac{\eta^o U_d}{\sigma_{eq}} \quad (3.7)$$

Table 3.2: Material properties of Newtonian fluid systems studied.

System	Suspending Fluid	Drop Fluid	h (mm)	ρ (kg/m ³)	ρ_d (kg/m ³)	η^o (mPa.s)	η_d^o (mPa.s)	σ_{eq} (mN/m)
GW1-1	80% glycerol-water solution	Air	10	1089	1.2	57	0.02	49
GW2-1	90% glycerol-water solution	Air	10	1137	1.2	96	0.02	53
GW3-1	95% glycerol-water solution	Air	10	1196	1.2	262	0.02	61
GW1-2	80% glycerol-water solution	Air	15	1089	1.2	57	0.02	49
GW2-2	90% glycerol-water solution	Air	15	1137	1.2	96	0.02	53
GW3-2	95% glycerol-water solution	Air	15	1196	1.2	262	0.02	61
GW4-2	99% glycerol-water solution	Air	15	1219	1.2	328	0.02	65
GW1-3	80% glycerol-water solution	Air	20	1089	1.2	57	0.02	49
GW3-3	95% glycerol-water solution	Air	20	1196	1.2	262	0.02	61
GW4-3	99% glycerol-water solution	Air	20	1219	1.2	328	0.02	65

Table 3.3: Material properties of viscoelastic fluid systems studied.

System	Suspending Fluid	Drop Fluid	h (mm)	ρ (kg/m ³)	ρ_d (kg/m ³)	η^o (mPa.s)	η_d^o (mPa.s)	σ_{eq} (mN/m)
PAM1-2	0.1% PAM solution	Air	15	951	1.2	1650	0.02	68
PAM2-2	0.25% PAM solution	Air	15	994	1.2	11830	0.02	77
PAM3-2	0.1% PAM in 50% glycerol-water solution	Air	15	1086	1.2	9780	0.02	66

Table 3.4: Material properties of surfactant systems studied.

System	Suspending Fluid	Drop Fluid	h (mm)	ρ (kg/m ³)	ρ_d (kg/m ³)	η^o (mPa.s)	η_d^o (mPa.s)	σ_{eq} (mN/m)
TX1-1	10 ppm Triton X-100 in 95% glycerol-water	Air	10	1186	1.2	262	0.02	61
TX2-1	100 ppm Triton X-100 in 95% glycerol-water	Air	10	1180	1.2	262	0.02	46
TX1-2	10 ppm Triton X-100 in 95% glycerol-water	Air	15	1186	1.2	262	0.02	61
TX2-2	100 ppm Triton X-100 in 95% glycerol-water	Air	15	1180	1.2	262	0.02	46
TX3-2	1000 ppm Triton X-100 in 95% glycerol-water	Air	15	1203	1.2	262	0.02	39

The Reynolds number gives the relative magnitude of the inertial forces to the viscous forces, the Bond number gives the ratio of gravitational forces to interfacial forces and the capillary number shows the relative significance of viscous forces to the interfacial

forces. The ranges of the dimensionless numbers used in our experiments are shown in Table 3.5. Since $Ca > 0.04$ for most of the bubbles in our experiments, the assumption that the bubbles are axisymmetric is valid [19].

Table 3.5: Dimensionless values of parameters in the experiment.

System	$\gamma \times 10^3$	$\lambda \times 10^3$	κ	Bo	Re	Ca
GW1-1	1.10	0.32	0.2 – 1.1	5.4	3.9 – 5.8	0.05 – 0.07
GW2-1	1.06	0.19	0.3 – 1.1	5.3	1.5 – 3.5	0.05 – 0.11
GW3-1	1.00	0.07	0.2 – 1.3	4.8	0.5 – 1.1	0.09 – 0.20
GW1-2	1.10	0.32	0.3 – 1.4	12.3	13.5 – 28.7	0.11 – 0.23
GW2-2	1.06	0.19	0.2 – 1.5	11.8	4.5 – 11.3	0.09 – 0.23
GW3-2	1.00	0.07	0.2 – 1.1	10.8	0.8 – 3.1	0.11 – 0.38
GW4-2	0.98	0.05	0.2 – 1.5	10.3	0.2 – 1.7	0.05 – 0.30
GW3-3	1.00	0.07	0.2 – 1.7	19.2	1.7 – 6.7	0.17 – 0.63
GW4-3	0.98	0.05	0.2 – 1.5	18.4	0.8 – 3.8	0.12 – 0.51
PAM1-2	1.26	0.01	0.2 – 1.5	7.7	0.1 – 0.7	1.03 – 3.95
PAM2-2	1.21	0.00	0.5 – 1.4	7.1	0.02 – 0.06	4.87 – 14.20
PAM3-2	1.10	0.00	0.3 – 1.5	9.1	0.01 – 0.07	2.45 – 11.65
TX1-1	1.01	0.07	0.1 – 0.8	4.8	0.4 – 0.9	0.08 – 0.17
TX2-1	1.02	0.07	0.2 – 1.2	6.3	0.4 – 1.1	0.12 – 0.26
TX1-2	1.01	0.07	0.2 – 1.4	10.7	0.5 – 2.5	0.07 – 0.31
TX2-2	1.02	0.07	0.2 – 1.4	14.1	0.6 – 2.9	0.11 – 0.49
TX3-2	1.00	0.07	0.2 – 1.6	17.0	1.1 – 2.7	0.23 – 0.51

CHAPTER IV

RESULTS AND DISCUSSION

The results for the motion of bubbles rising in a Newtonian and viscoelastic fluids as well as surfactant solutions are presented in the following sections. In all of the experimental results presented in this thesis, the bubbles remained near the centerline as they passed through the capillary tube. The terminal velocity as a function of the bubble volume for the GW1-1 system is presented in Figure 4.1 along with a comparison for the same run repeated with the capillary rotated by 90 degrees. The two data sets lie more or less on top of each other confirming that the data are reproducible and the bubbles remain more or less along the centerline of the capillary.

The edges of the images presented in this thesis do not correspond to the tube wall. The bubble shape is characterized by the length of the bubble, L , the width of the bubble, B , and the deformation parameter, Δ . The length and width of the bubble are defined as the maximum axial and radial dimension of the steady bubble profile made dimensionless with the capillary radius. The deformation parameter is defined as,

$$\Delta = \frac{(L - B)}{(L + B)} \quad (4.1)$$

For a circular bubble, $\Delta = 0$ and the deformation parameter is positive for a prolate bubble while the parameter is negative for an oblate bubble.

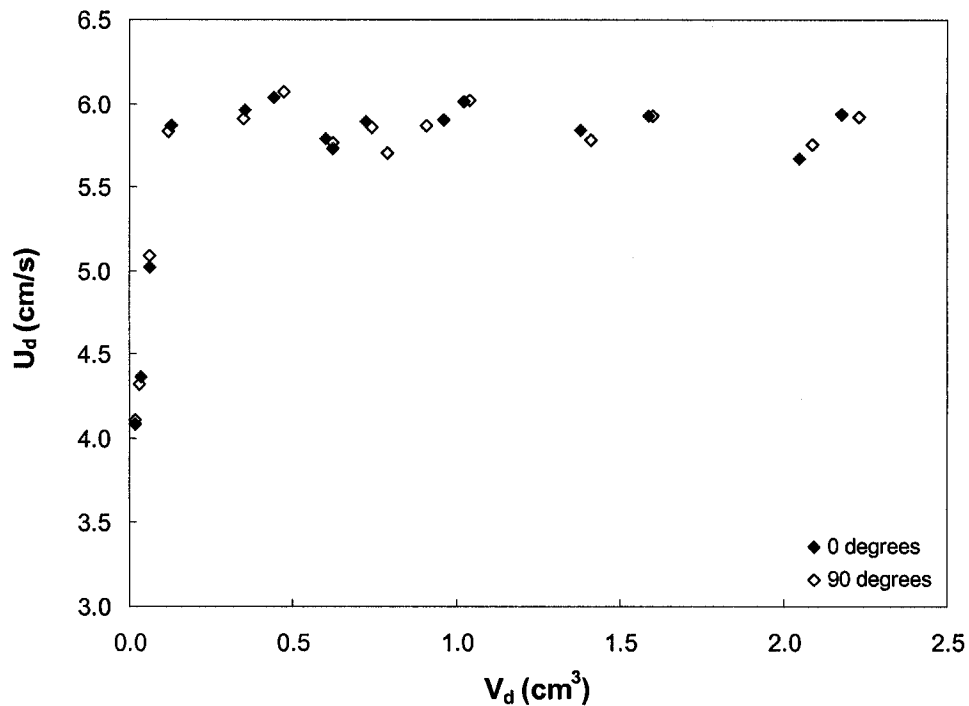


Figure 4.1: Terminal velocity as a function of the bubble volume for air bubbles rising in 80% glycerol-water solution in 10mm square capillary.

Newtonian Systems

The sample shapes of bubbles as a function of the bubble volume for the GW2-2 system are seen in Figure 4.2. The bubbles are nearly spherical at small volumes. As the bubble volume increases ($\kappa > 0.38$), the bubble loses its fore and aft symmetry. The bubble has a

positive curvature in the front and is flattened at the rear. As the bubble volume is further increased ($\kappa > 0.77$), a negative curvature develops at the rear end of the bubble. As the bubble volume is increased, the bubble becomes more elongated with higher positive curvature at the front of the bubble and negative curvature at the rear of the bubble.

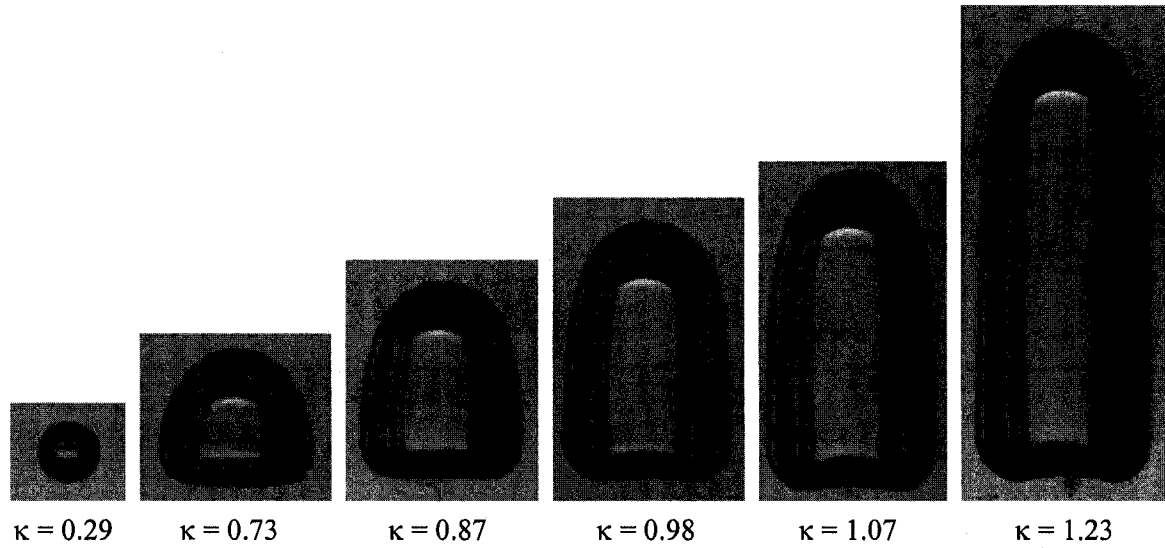


Figure 4.2: Steady shapes as a function of the dimensionless bubble size for air bubbles rising in 90% glycerol-water solution in 15 mm square capillary ($Bo = 11.83$).

The dimensionless length and width of the bubbles as a function of the dimensionless bubble size, κ for the GW2-2 system are shown in Figure 4.3. The data points corresponding to the bubble shapes shown in Figure 4.2 are marked with open square symbols in Figures 4.3 - 4.9. The length and width of the bubble increase almost linearly as a function of bubble size for small bubble volumes. As the volume increases, the width of the bubble reaches an upper bound less than the size of the square capillary, $2R_H$. At this point the width remains unchanged and the bubble length increases linearly at a much faster rate. The length of the bubble as a function of the width of the bubbles

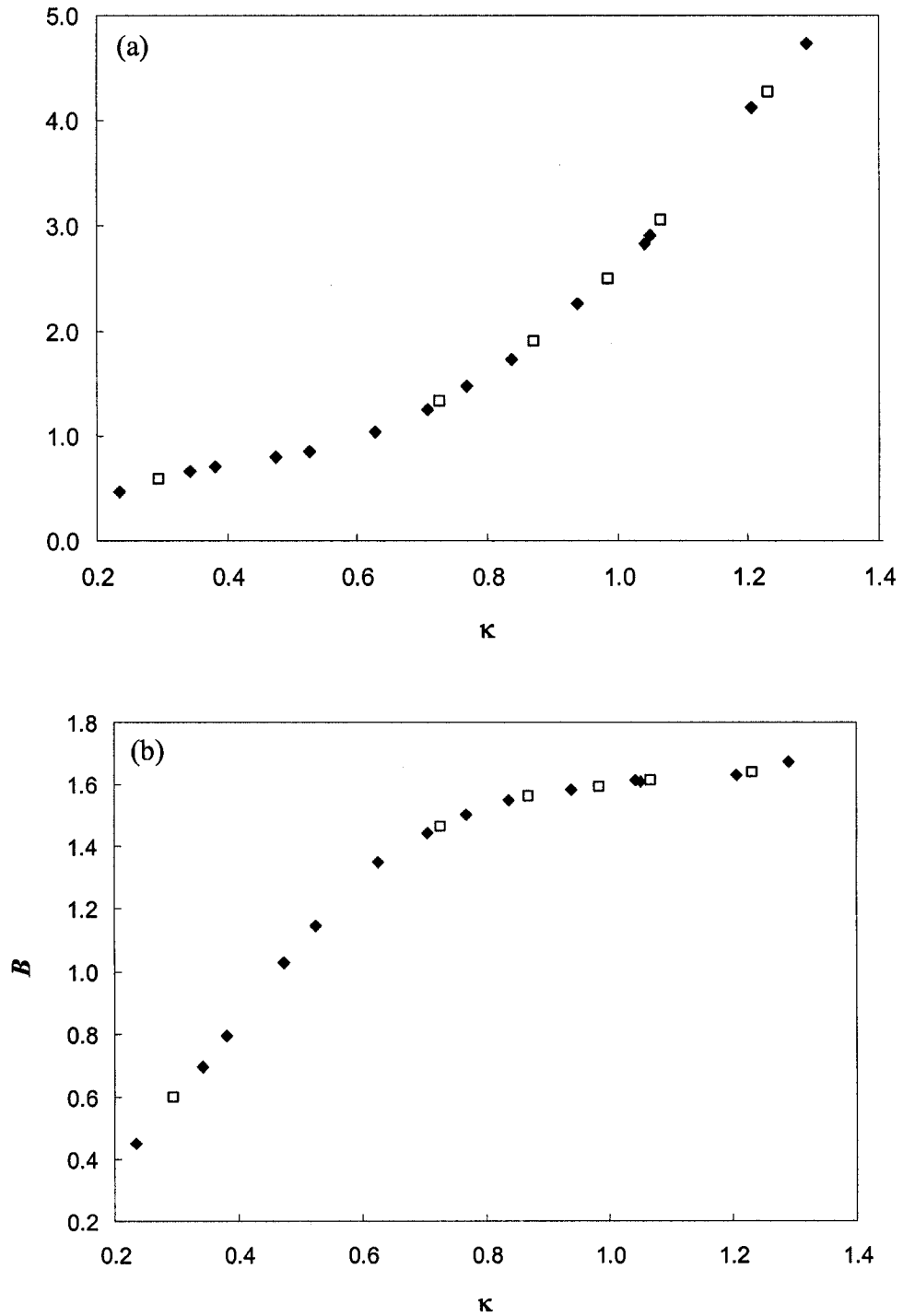


Figure 4.3: The (a) length and (b) width of bubbles as a function of bubble size for bubbles rising in 90% glycerol-water solution in 15 mm square capillary. The open symbols correspond to the bubbles presented in Figure 4.2.

for the GW2-2 system is shown in Figure 4.4. The dashed line represents the curve for a spherical bubble. The deformation parameter, Δ as a function of bubble size, κ , is shown in Figure 4.5. For small bubble sizes the bubbles are nearly spherical. As the bubble size increases, the bubbles become oblate with bubbles elongated perpendicular to the direction of flow. For $\kappa > 0.77$, the bubbles become prolate and for $\kappa > 1.21$, the bubble does not grow in the radial direction and any increase in the volume results in increasing the length of the bubble. The minimum film thickness between the bubble wall and the capillary wall made dimensionless with the hydraulic radius, δ , is presented in Figure 4.6 as a function of the dimensionless bubble size for the GW2-2 system. The film thickness reduces as the bubble size increases and appears to reach a constant film thickness for long bubbles as observed by Bretherton [6].

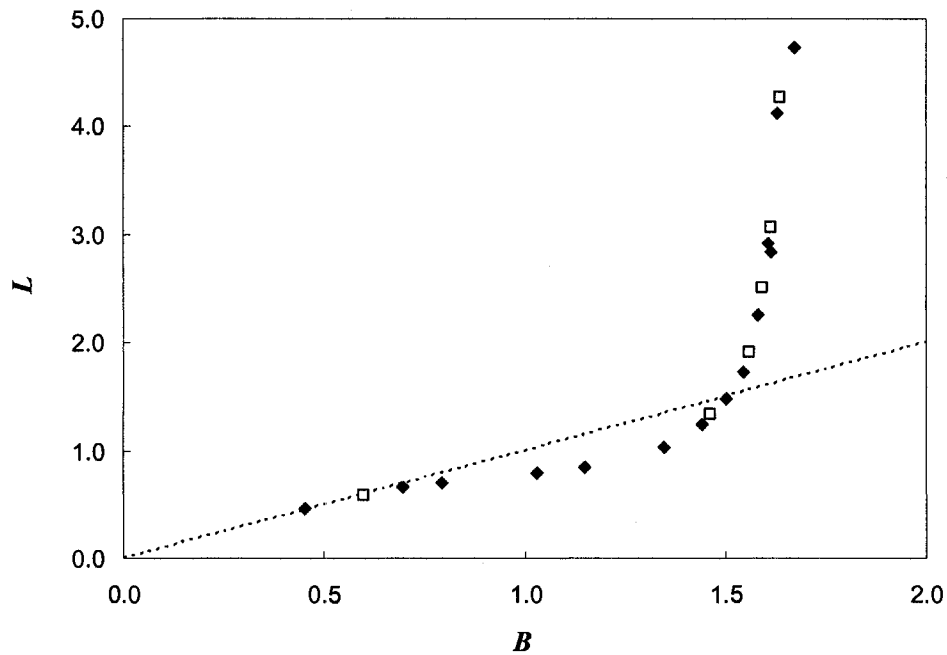


Figure 4.4: The length of the bubble as a function of the bubble width for bubbles rising in 90% glycerol-water solution in 15 mm square capillary. The dashed line represents the curve for a circular bubble.

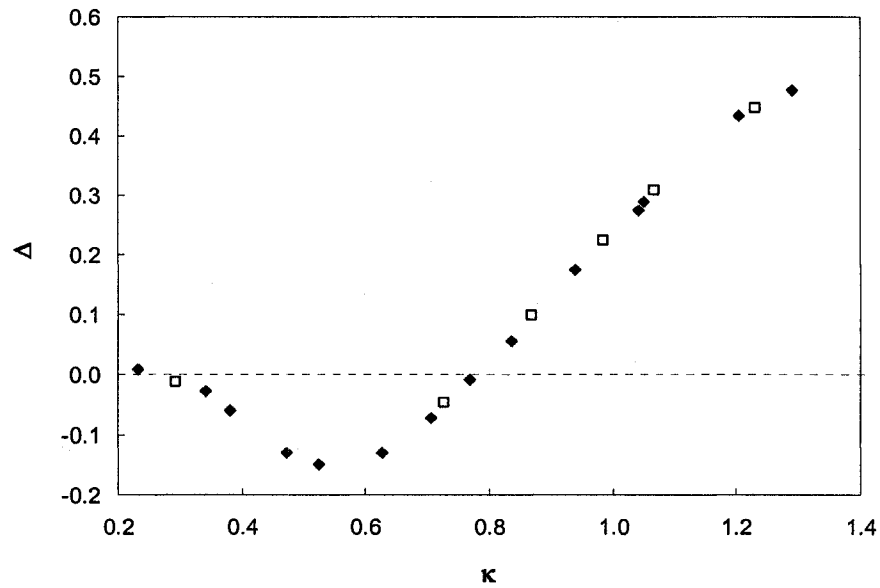


Figure 4.5: The deformation parameter as a function of the dimensionless bubble size for bubbles rising in 90% glycerol-water solution in 15 mm square capillary. The open symbols correspond to the bubbles presented in Figure 4.2.

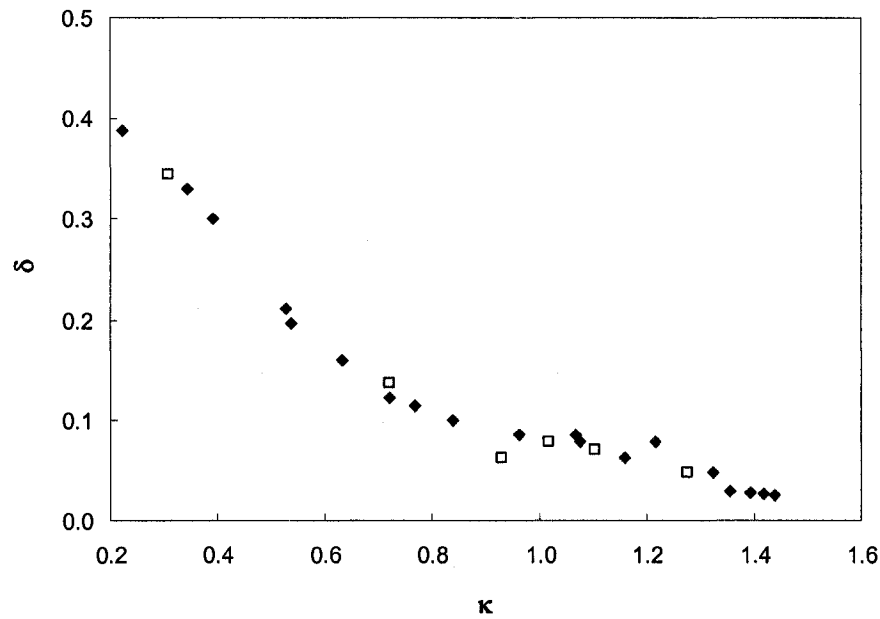


Figure 4.6: The dimensionless film thickness as a function of the dimensionless bubble size for bubbles rising in 90% glycerol-water solution in 15 mm square capillary. The open symbols correspond to the bubbles presented in Figure 4.2.

The dimensional velocity of the bubble, U_d , and the dimensionless steady velocity of the bubble, U , for GW2-2 system are shown in Figures 4.7 and 4.8 respectively. The dimensional steady bubble velocity is made dimensionless with the characteristic velocity, $(\rho - \rho_d)gR_H^2/\mu$. The data points corresponding to the bubble shapes shown in Figure 4.2 are marked with open square symbols in Figures 4.7 through 4.9. For small bubble volumes, the velocity increases as the bubble volume increases due to predominantly buoyancy effects. As the bubble volume increases, wall effects begin to dominate and the bubble velocity reduces as the drop volume increases. Beyond a critical bubble volume ($V_d = 2.75 \text{ cm}^3$, $\kappa = 1.16$), the bubble velocity is independent of the bubble size similar to a Taylor bubble. The dimensionless bubble size is consistent with the critical bubble volume at which the film thickness becomes constant.

The effects of the wall can be determined by comparing the velocity of the bubble to the velocity of a spherical bubble of similar volume rising with the Hadamard-Rybczinski velocity, $U_{HR} = (\rho - \rho_d)ga^2/3\mu$, where a is the radius of a spherical bubble of the same volume. The dimensionless velocity, $U^* = U_d/U_{HR}$, as a function of the bubble volume for the GW2-2 system is shown in Figure 4.9. For the smallest size bubble shown in Figure 4.9, corresponding to $\kappa = 0.23$, the bubble is slightly prolate ($\Delta = 0.016$) with a terminal velocity that is almost half the terminal velocity expected for a similar sized spherical bubble in quiescent fluid. The reduction in the mobility of the bubble is due to the presence of walls near the bubble.

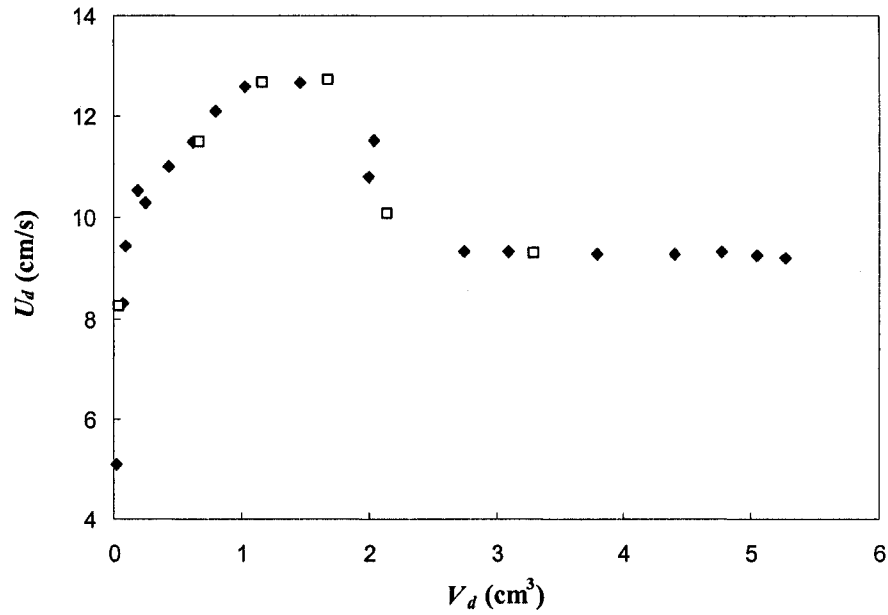


Figure 4.7: Terminal velocity as a function of the bubble volume for air bubbles rising in 90% glycerol-water solution in 15 mm square capillary. The open symbols correspond to the bubbles presented in Figure 4.2.

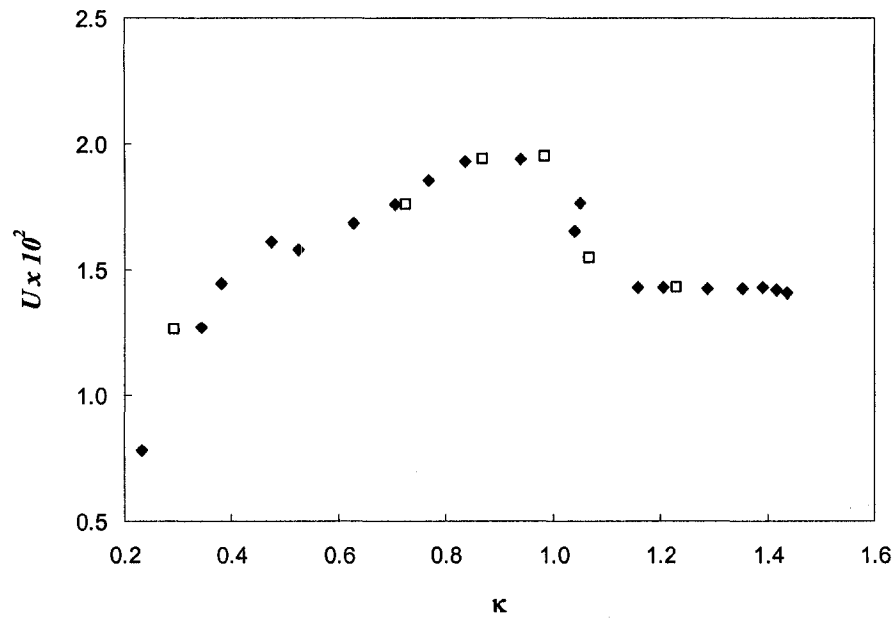


Figure 4.8: Dimensionless terminal velocity as a function of the dimensionless bubble size for air bubbles rising in 90% glycerol-water solution in 15 mm square capillary. The open symbols correspond to the bubbles presented in Figure 4.5.

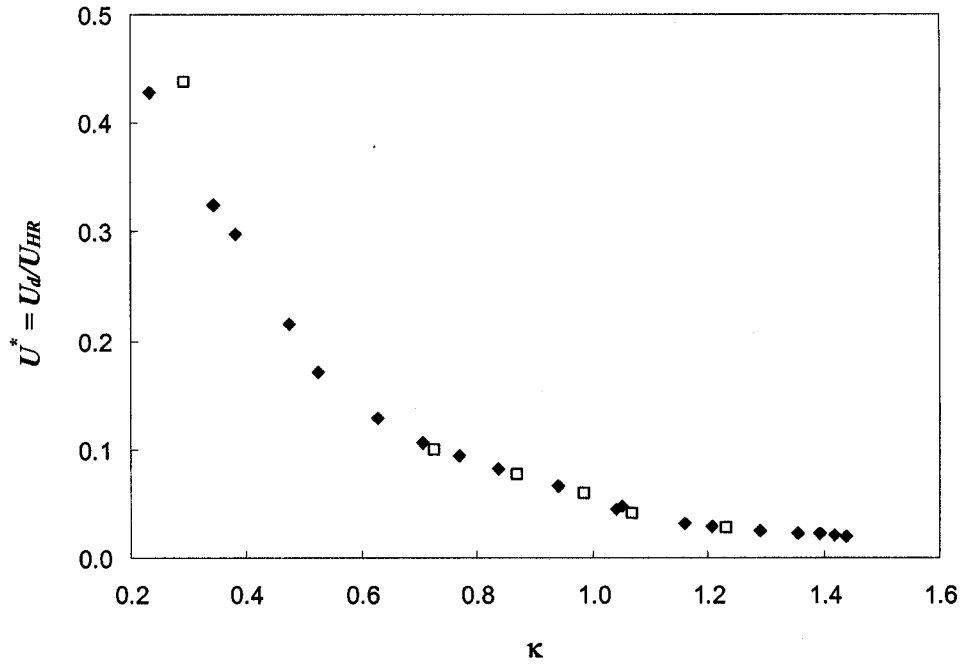
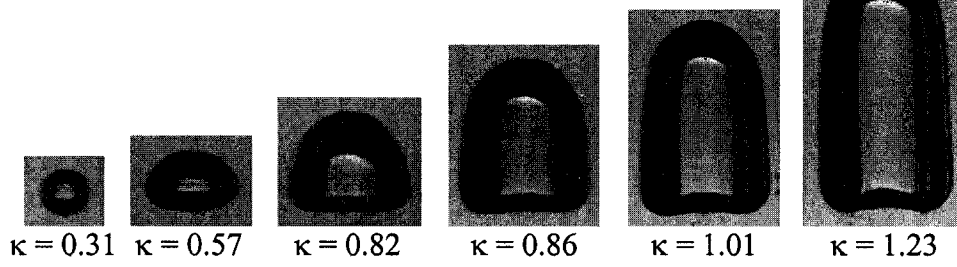


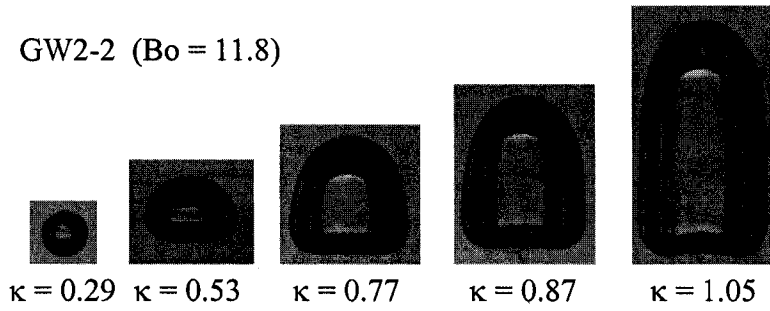
Figure 4.9: Steady dimensionless velocity of air bubbles as a function of the dimensionless bubble size for air bubbles rising in 90% glycerol-water solution in 15 mm square capillary. The open symbols correspond to the bubbles presented in Figure 4.2.

The effect of changing the bulk fluid viscosity on the shapes of bubbles rising in the 15 mm square capillary is shown in Figure 4.10. The bulk fluids used are 80% glycerol-water (GW1-2), 90% glycerol-water (GW2-2), 95% glycerol-water (GW3-2), and 99% glycerol-water (GW4-2). As the viscosity of the bulk fluid increases, air bubbles of the same volume become more prolate. For the GW1-2 and GW2-2, as the bubble volumes increase, a reentrant cavity is seen at the rear of the bubble. For the higher viscosity bulk fluids (GW3-2 and GW4-2), a negative curvature at the rear of the bubble is not observed. There appears to be a critical bulk viscosity above which the reentrant cavity is not observed for the bubble sizes investigated.

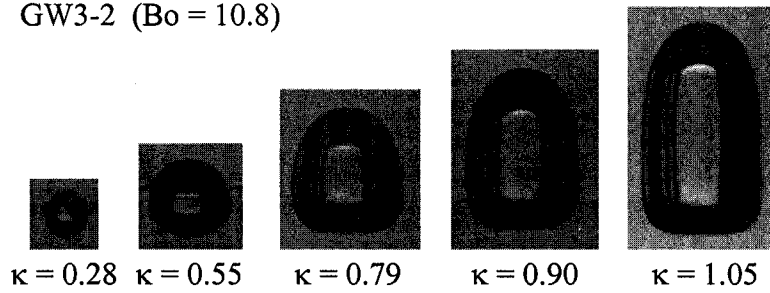
GW1-2 ($Bo = 12.3$)



GW2-2 ($Bo = 11.8$)



GW3-2 ($Bo = 10.8$)



GW4-2 ($Bo = 10.3$)

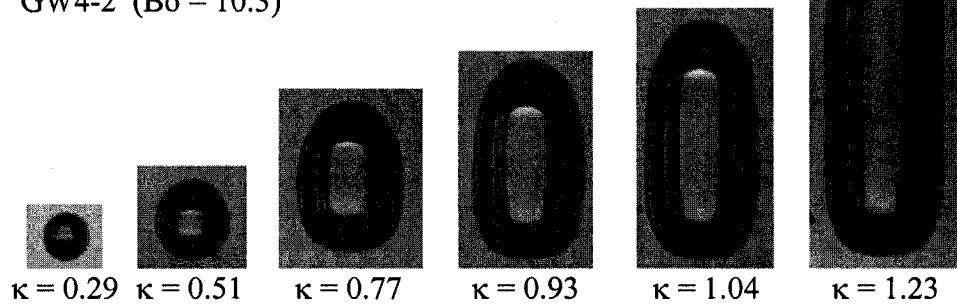


Figure 4.10: Steady shapes for air bubbles as a function of the dimensionless bubble size for air bubbles rising in GW1-2, GW2-2, GW3-2, and GW4-2 systems.

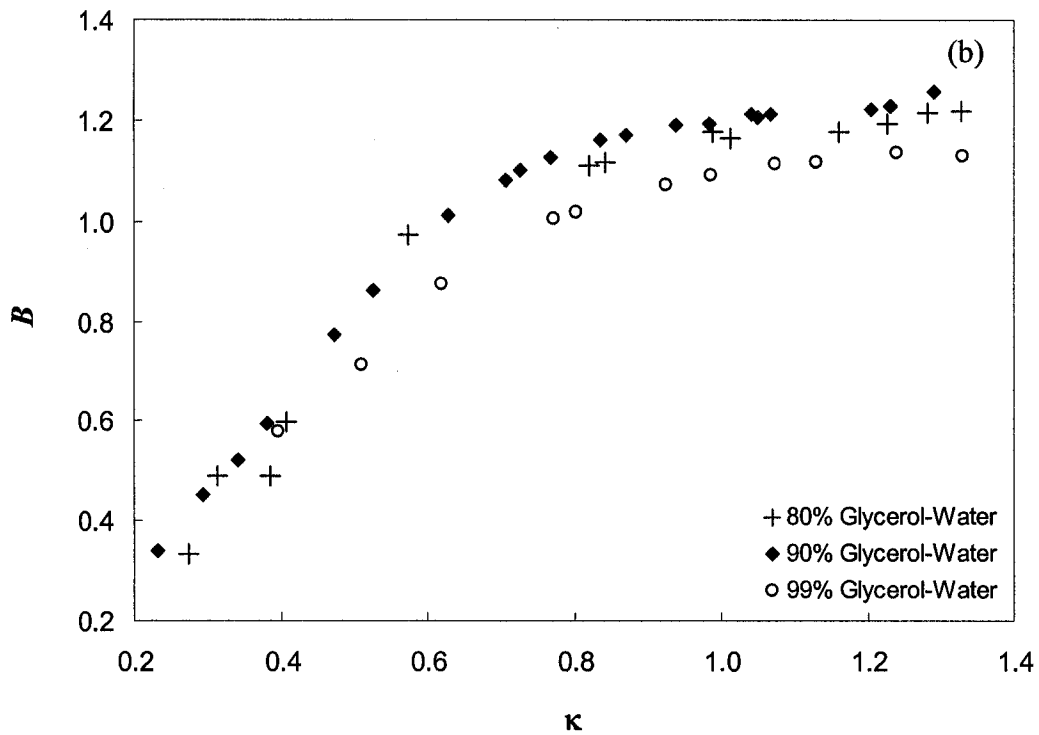
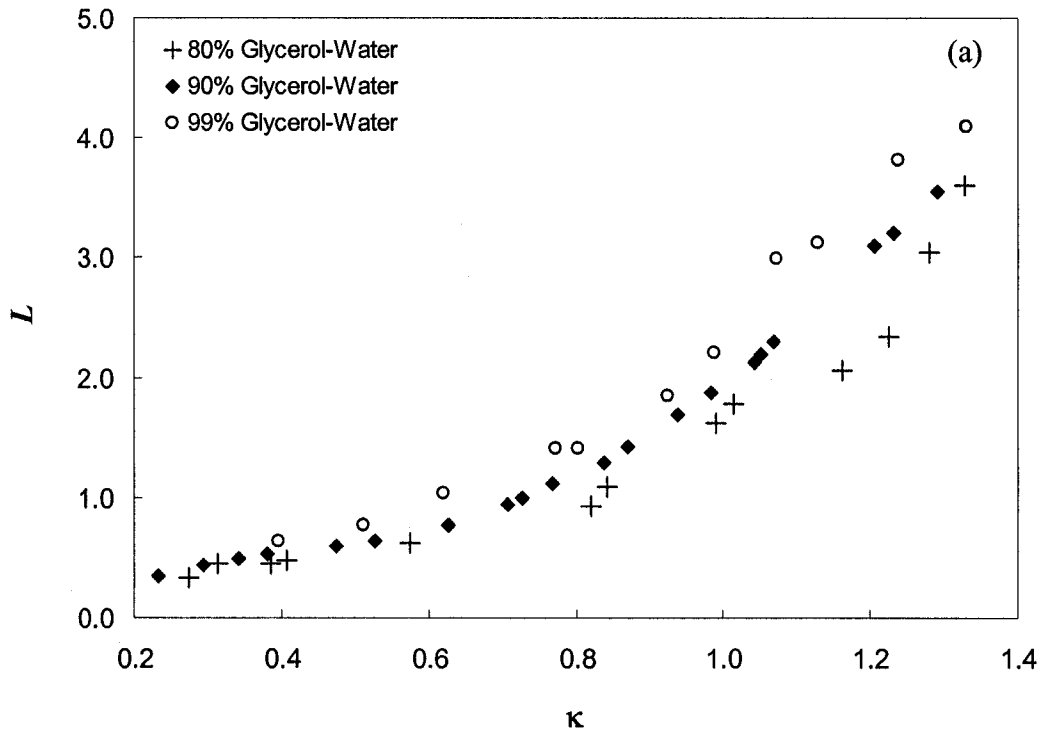


Figure 4.11: The (a) length and (b) width of bubbles as a function of bubble size for bubbles rising in 80%, 90%, and 99% glycerol-water solution in 15 mm square capillary.

The dimensionless length and width of the steady air bubbles rising in the GW1-2, GW2-2, and the GW4-2 systems are shown in Figure 4.11. The length of the bubbles increases as the viscosity of the bulk fluid increases while the width of the bubble appears to decrease as the viscosity of the bulk fluid increases. The length versus the width of the bubble and the deformation parameter as a function of bubble size is seen in Figures 4.12 and 4.13. In all three cases, initially the bubbles are nearly spherical. For the bubbles rising in the fluids below the critical bulk viscosity, the bubbles are oblate for the intermediate bubble volumes and eventually become prolate for higher bubble volumes. The bubbles rising in the 99% glycerol-water solution are not oblate for any bubble volume. As expected, the minimum film thickness for the bubbles rising in the higher

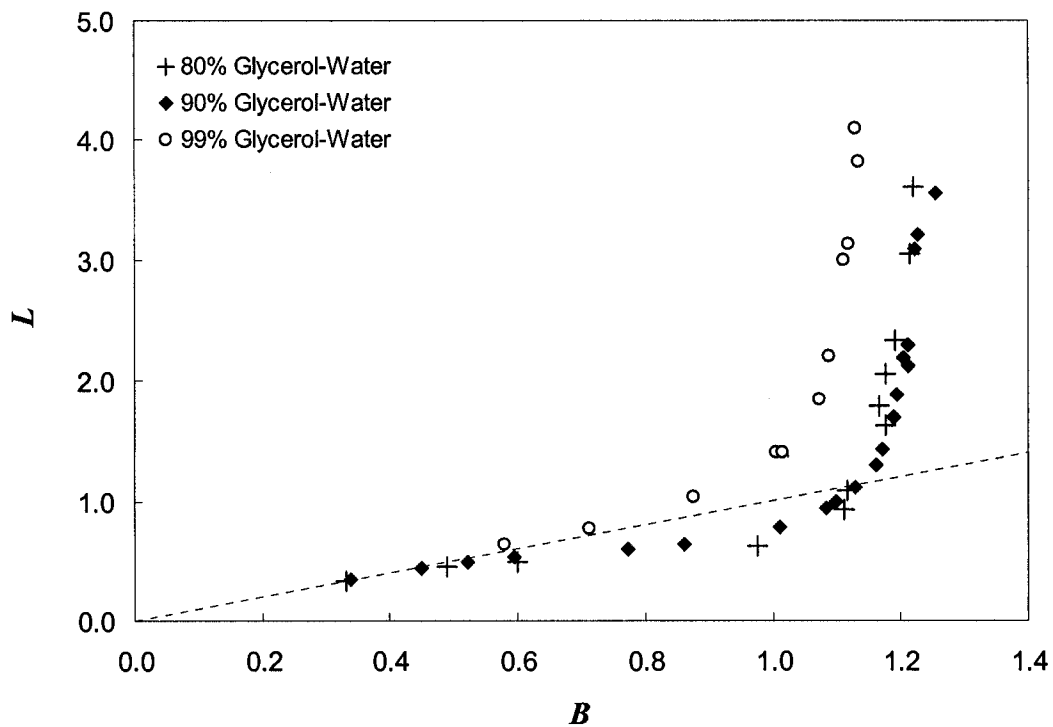


Figure 4.12: Comparison of the length of the bubble as a function of the bubble width for bubbles rising in 80%, 90%, and 99% glycerol-water solutions in 15 mm square capillary. The dashed line represents the curve for a circular bubble.

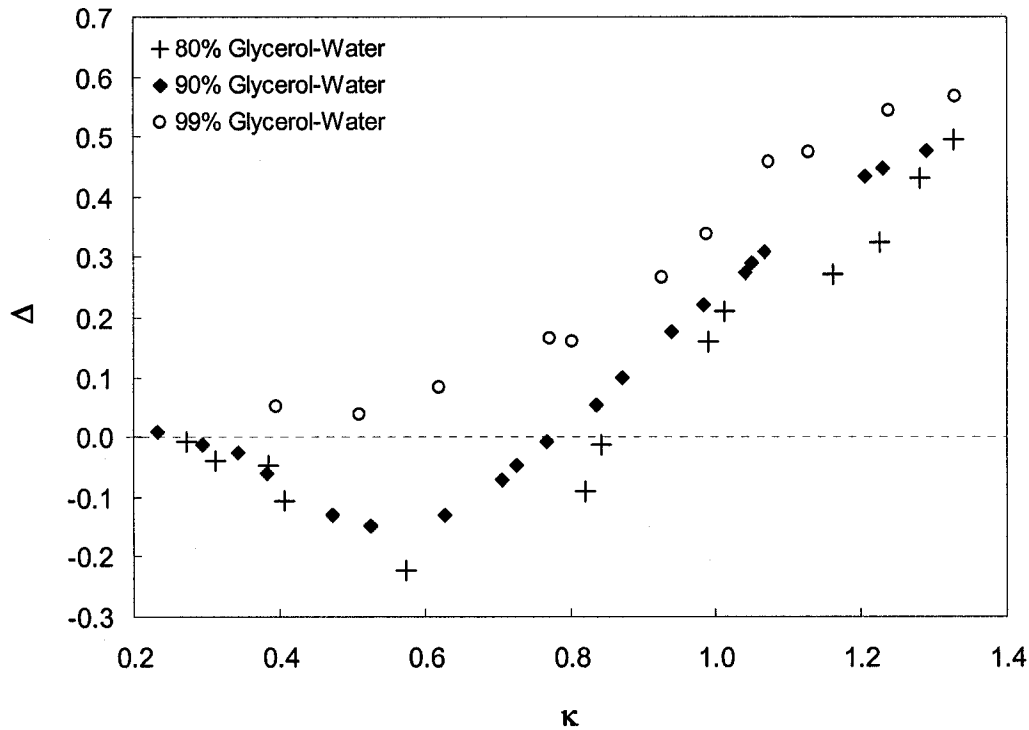


Figure 4.13: Comparison of the deformation parameter as a function of the dimensionless bubble size for bubbles rising in 80%, 90%, and 99% glycerol-water solutions in 15 mm square capillary.

viscosity fluids is more than the film thickness for the bubbles rising in the lower viscosity fluids (see Figure 4.14).

The effect of changing the bulk fluid viscosity on the terminal velocity of the air bubbles is seen in Figures 4.15 through 4.17. For all values of the bulk viscosity in the 15 mm tube, the velocity-volume curve shows a local maximum in the terminal velocity for lower bubble volumes. However, as the viscosity of the bulk phase increases, the ratio of the maximum bubble velocity for small bubbles to the steady velocity of long bubbles reduces. For example, $U_{d,max}/U_d|_{d \rightarrow \infty} = 1.51$ for 80% glycerol-water system while

$U_{d,\max}/U_d|_{a\rightarrow\infty} = 1.41$ for the 99% glycerol-water system. Furthermore, as the viscosity of the bulk fluid is increased, the steady velocity of bubbles is reduced even though the shape of the bubbles is more prolate for higher viscosity bulk fluids. This is due to the increased drag experienced by the bubbles rising in a higher viscosity fluid. The effect of bulk viscosity on the dimensional bubble velocity can be eliminated by non-dimensionalizing the bubble velocity with the characteristic velocity scale, $(\rho - \rho_d)gR_H^2/\mu$ (see Figure 4.16). The velocity-volume curves for the 80% and 90% glycerol-water systems can be superimposed while the velocity-volume curve for the 99% glycerol-water system is higher than the curves for the GW1-2 and GW2-2 systems.

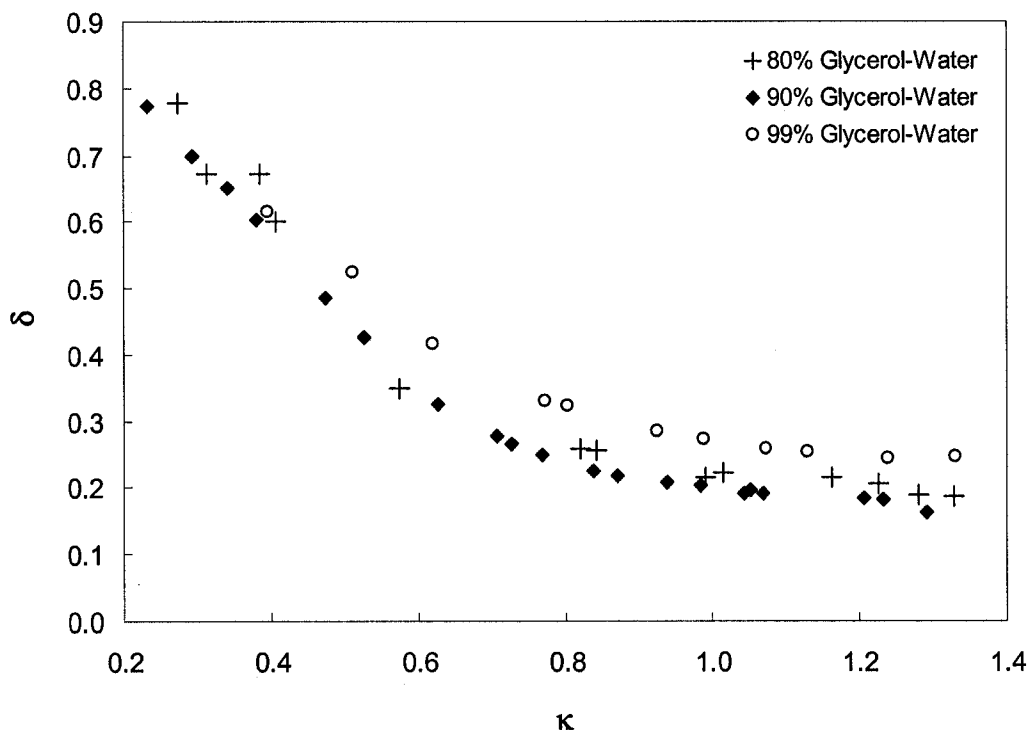


Figure 4.14: Comparison of the dimensionless film thickness as a function of the bubble size for bubbles rising in 80%, 90%, and 99% glycerol-water solutions in a 15 mm square capillary.

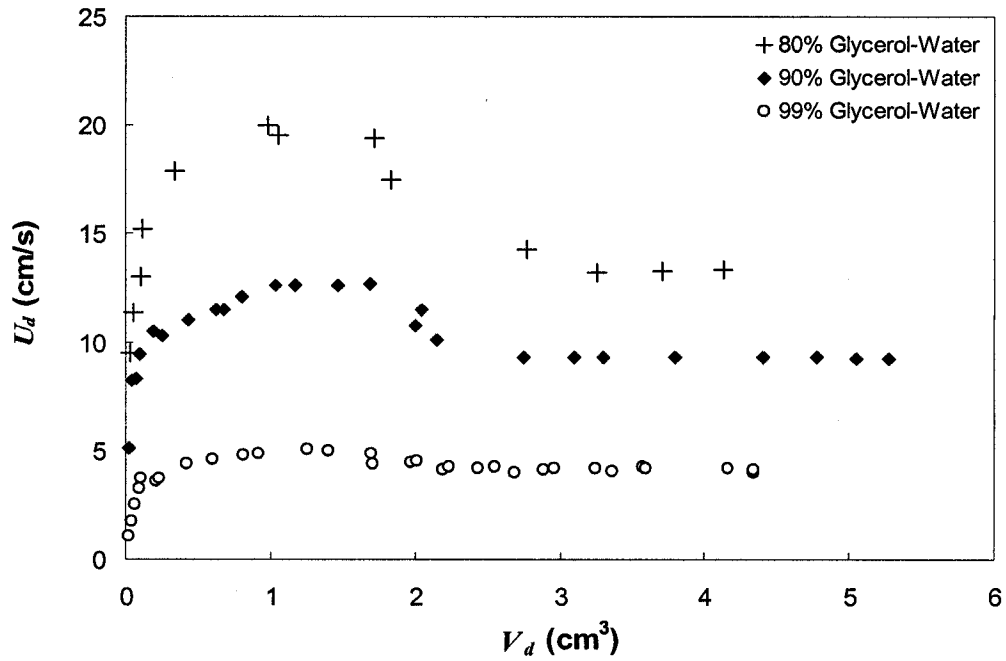


Figure 4.15: Comparison of terminal velocity as a function of the bubble volume for air bubbles rising in 80%, 90%, and 95% glycerol-water solution in 15 mm square capillary.

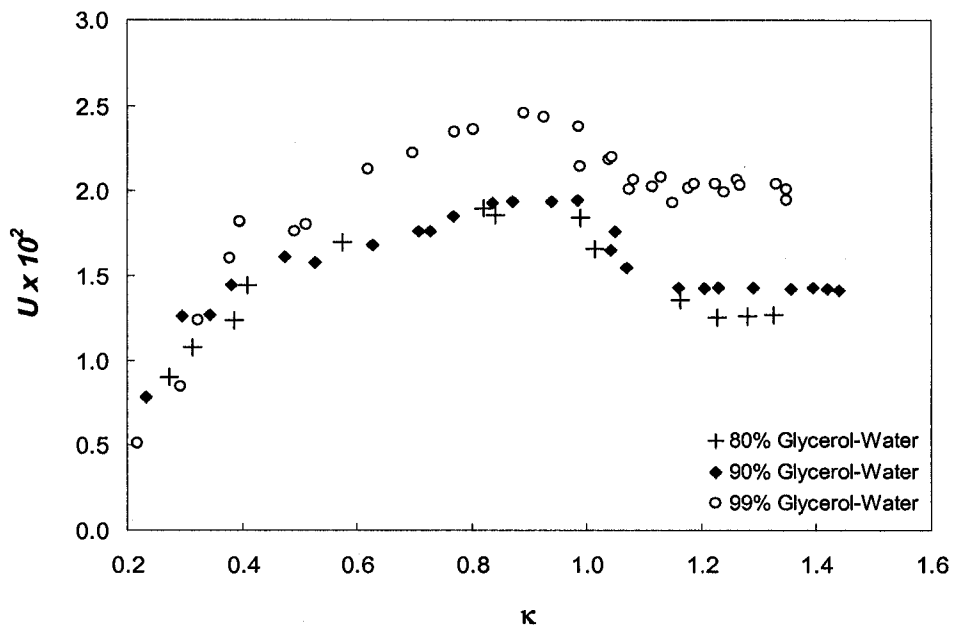


Figure 4.16: Comparison of dimensionless terminal velocity as a function of the bubble size for air bubbles rising in 80%, 90%, and 99% glycerol-water solutions in 15 mm square capillary.

The steady bubble velocities made dimensionless with the Hadamard-Rybczinski velocity for spherical bubbles of the same volume shows marginal variation with the viscosity of the bulk phase.

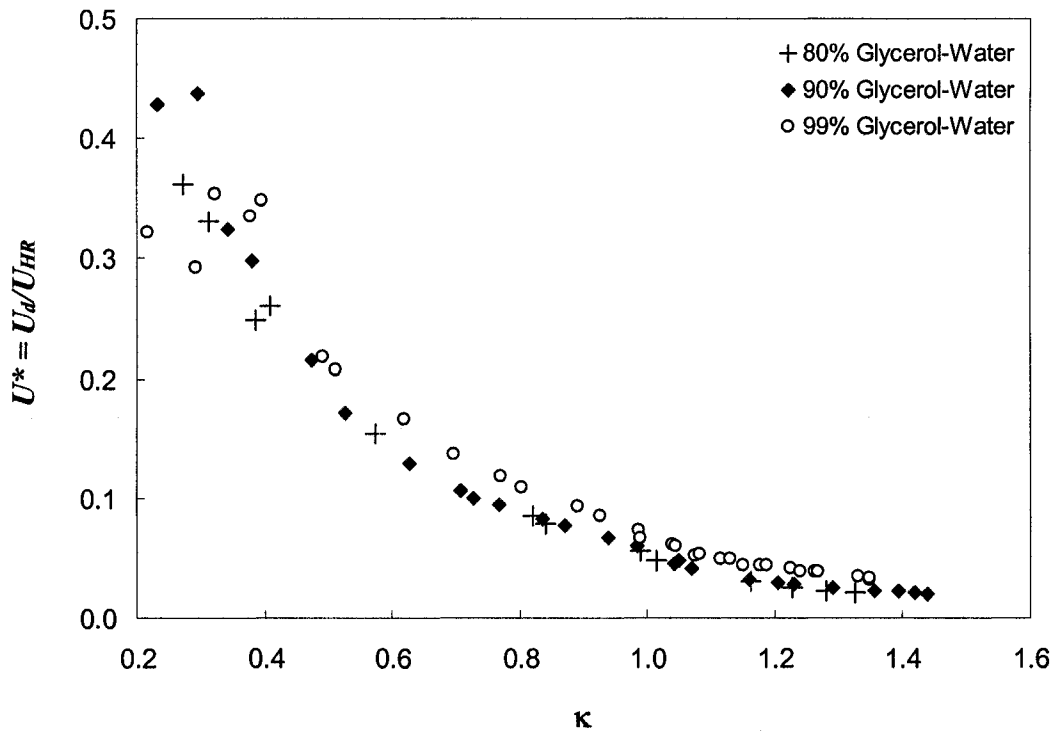


Figure 4.17: Comparison of steady dimensionless velocity of air bubbles as a function of the bubble size for air bubbles rising in 80%, 90%, and 99% glycerol-water solution in 15 mm square capillary.

The critical bulk viscosity at which the rising bubbles show a reentrant cavity at the rear stagnation point depends on the size of the square tube. The steady bubble shapes as a function of bubble size for bubbles rising in a 10 mm square channel filled with 80% glycerol-water are shown in Figure 4.18. Bubbles of all sizes show a positive curvature at the rear of the bubble suggesting that the critical bulk viscosity for the 10 mm tube is

lower than 57 cP. To test this hypothesis, air bubbles rising through the tube filled with distilled water were studied. Due to the very low viscosity of water (1cP), the bubbles were unstable and steady shapes were not observed. However, all the bubbles showed a reentrant cavity at the rear stagnation point suggesting that the critical bulk viscosity for the 10 mm square capillary lies between 1 cP and 57 cP. The critical bulk viscosity below which the bubbles start showing a negative curvature at the rear of the bubble increases as the tube size increases. For motion of bubbles in a 20 mm tube, the reentrant cavity is observed for viscosities as high as 328 cP (see Figure 4.20).

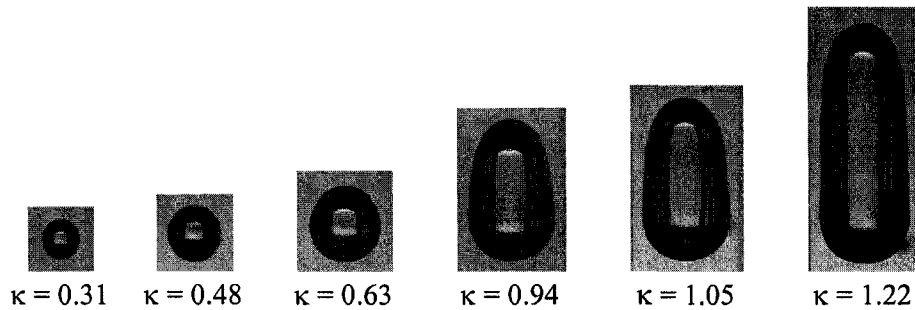


Figure 4.18: Steady shapes as a function of the dimensionless bubble size for GW1-1 system with bubbles showing no reentrant cavity.

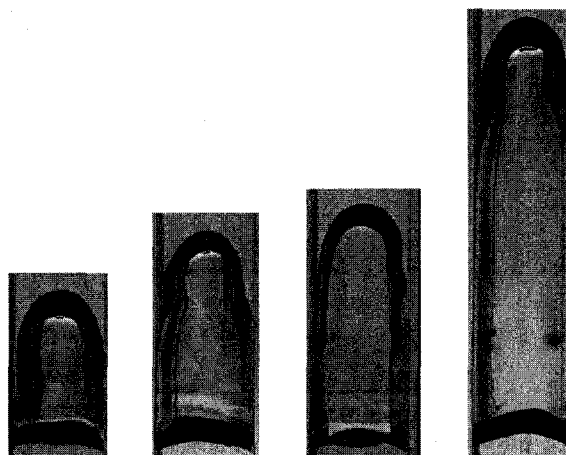


Figure 4.19: Unsteady shapes for varying bubble sizes for air bubbles rising in water showing a reentrant cavity.

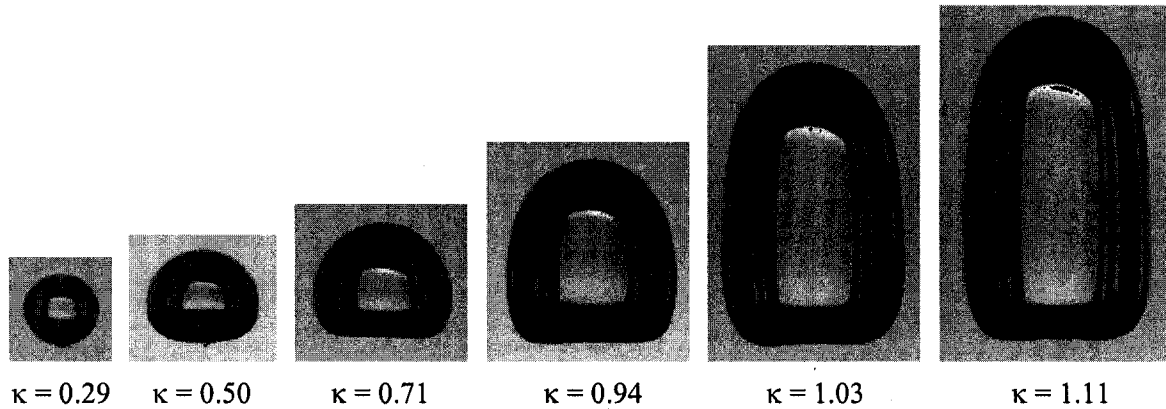


Figure 4.20: Steady bubble shapes as a function of the dimensionless bubble size for GW4-3 with bubbles showing a reentrant cavity.

The characteristics of the velocity-volume curve are also affected by changing the tube size. The velocity-volume curve for air bubbles rising in 80% glycerol-water in 10 mm ($Bo = 5.4$) and 15 mm ($Bo = 12.3$) square tubes is seen in Figure 4.21. For the 10 mm system, the velocity-volume curve does not show a maximum velocity at lower bubble volumes. Instead, the bubble velocity increases monotonically with bubble volume and reaches a plateau. Borhan and Pallinti [5] observed both of the velocity-volume curve characteristics reported here for buoyancy-driven motion of air bubbles in circular tubes at vanishing Reynolds numbers. In their study, the existence of a maximum in the velocity-volume curve was observed for lower Bond number systems while a monotonic increase in the bubble velocity was observed for higher Bond number systems. These results are opposite to the results reported here. This difference may be attributed to the inertial effects as the Reynolds numbers for the bubbles in the GW1-1 and GW1-2 systems are between 3.9 and 28.7.

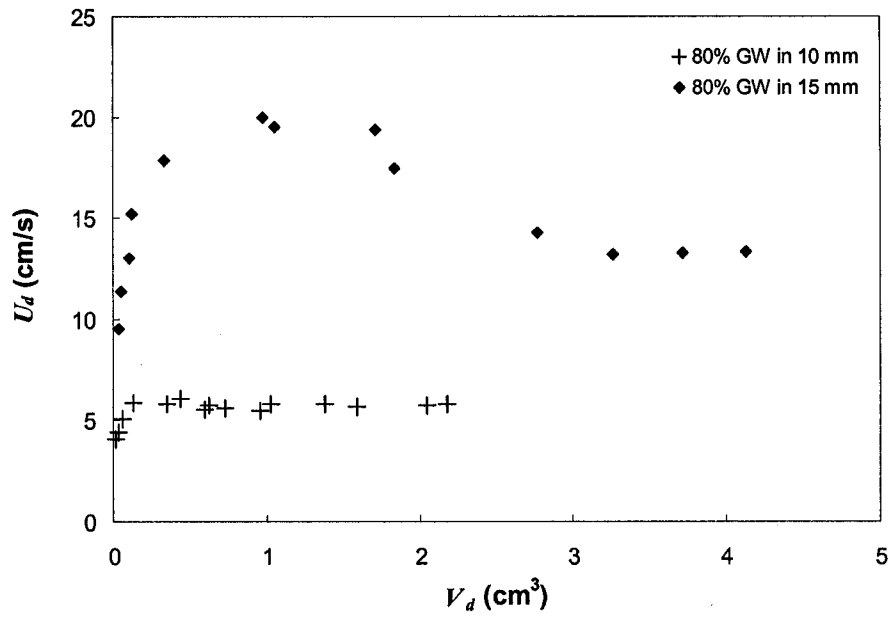


Figure 4.21: Comparison of terminal velocity as a function of the bubble volume for air bubbles rising in 80% glycerol-water solution in 10 mm and 15 mm square capillary.

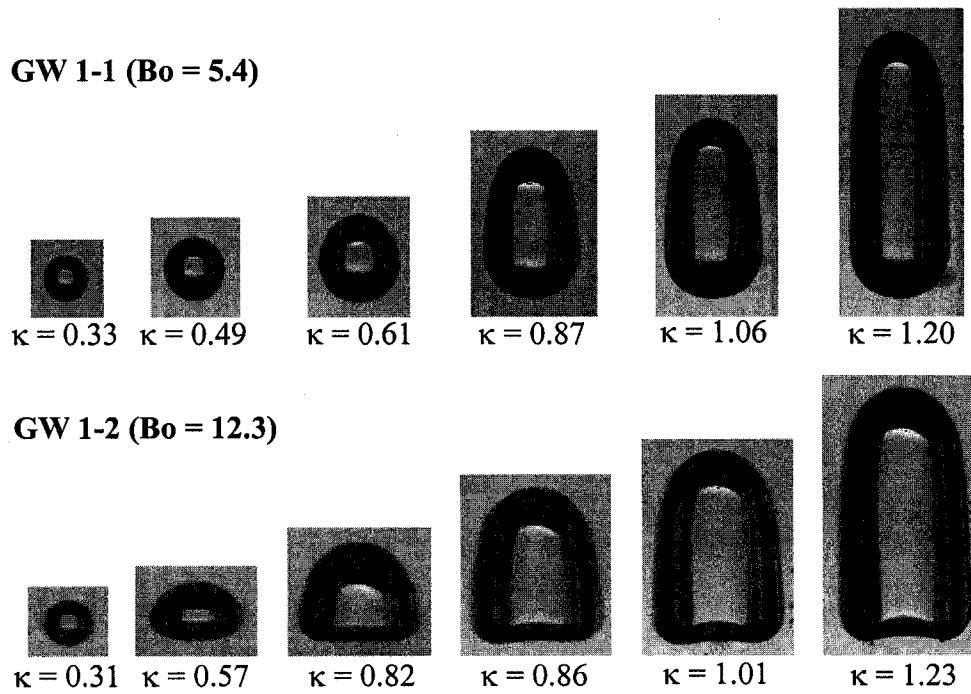


Figure 4.22: Steady bubble shapes as a function of the dimensionless bubble size for GW1-1 and GW1-2 systems.

The corresponding steady shapes for the GW1-1 and GW1-2 systems are shown in Figure 4.22. The images for the GW1-1 system are presented at 1.5 times the magnification of the GW1-2 system for ease of comparison. The more prolate shape of the bubbles in the 10 mm tube is not sufficient to overcome the additional drag experienced by the bubbles in the 10 mm tube as compared to the 15 mm tube.

Viscoelastic Systems

The steady shapes of bubbles rising in a 15 mm square capillary filled with 0.1% PAM solution is shown in Figure 4.23. The edges of the images presented in Figure 4.23 do not correspond to the tube wall. The bubble shapes obtained for bulk fluids with elastic effects are significantly different from those obtained for Newtonian bulk fluids. In the presence of elastic effects, even the smallest bubble ($\kappa = 0.48$) shows a pointed cusp at the trailing edge. Similar cusped shapes have been observed for bubbles translating in quiescent elastic fluids [11,16]. To the best of our knowledge, the cusps seen in this work are axisymmetric.

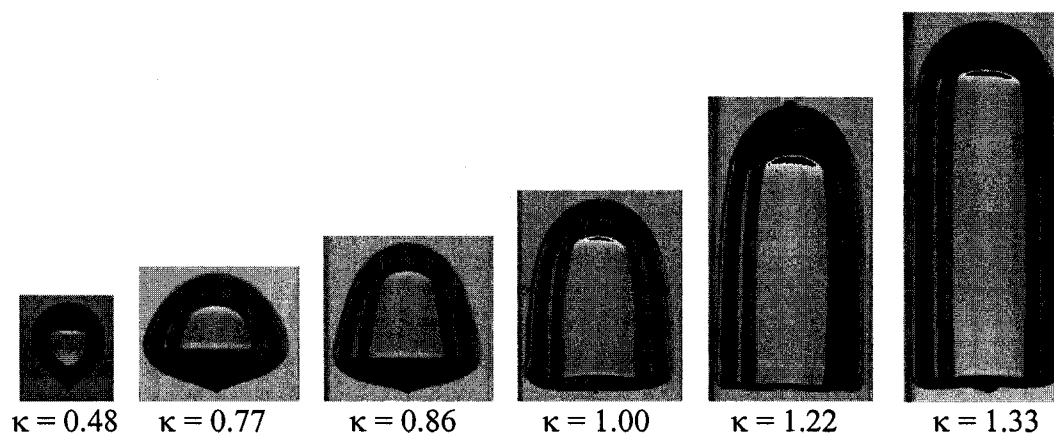


Figure 4.23: Steady shapes as a function of the dimensionless bubble size for air bubbles rising in 0.1% PAM solution in 15 mm square capillary ($Bo = 7.71$).

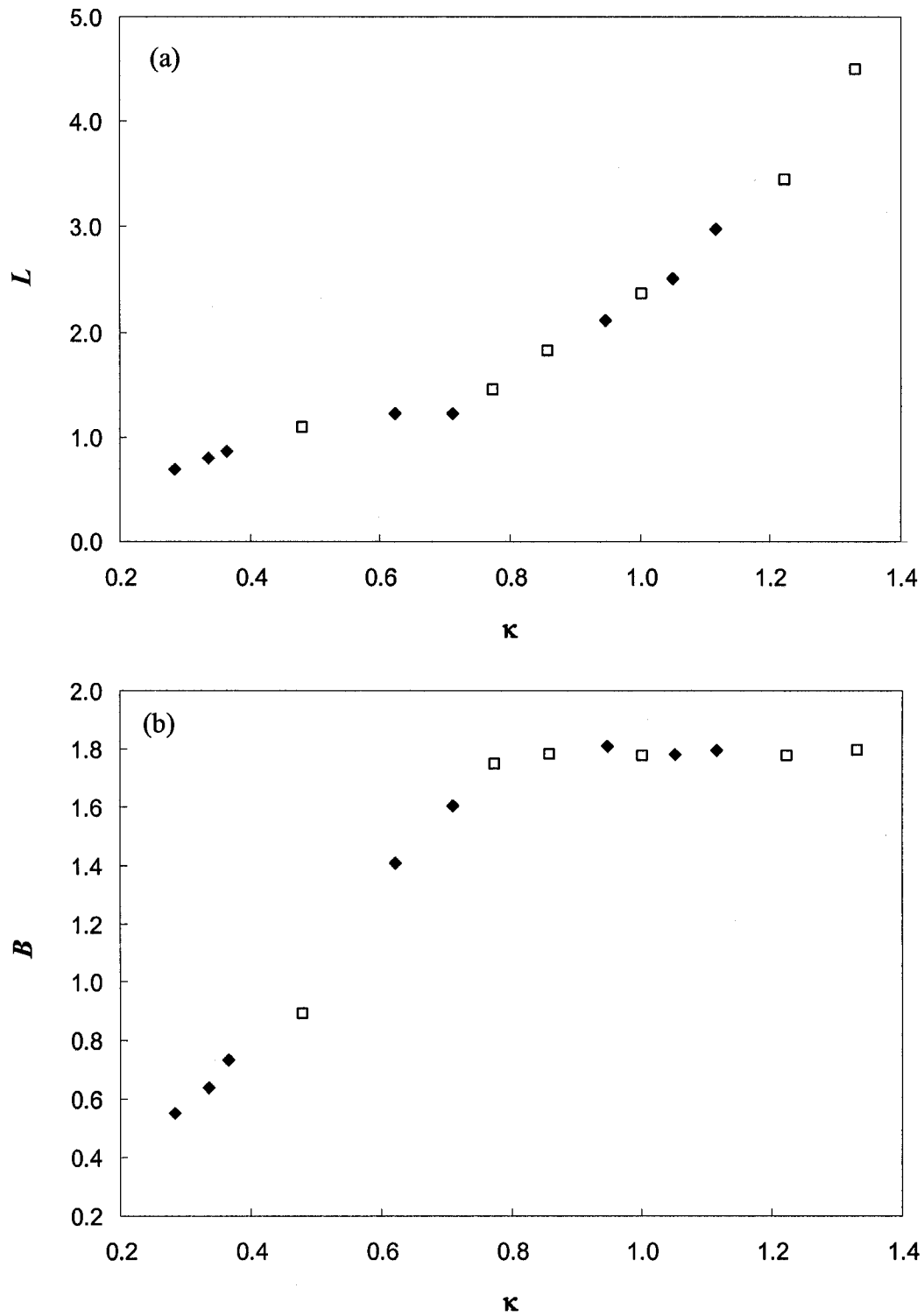


Figure 4.24: The (a) length and (b) width of bubbles as a function of bubble size for bubbles rising in 0.1% PAM solution in 15 mm square capillary. The open symbols correspond to the bubbles presented in Figure 4.23.

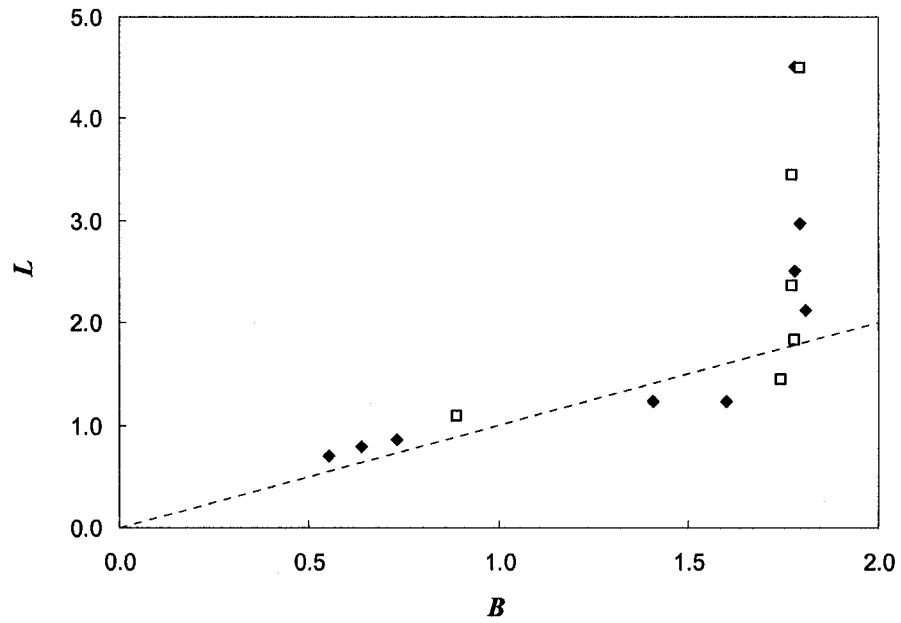


Figure 4.25: The length of the bubble as a function of the bubble width for bubbles rising in 0.1% PAM solution in 15 mm square capillary. The dashed line represents the curve for a spherical bubble.

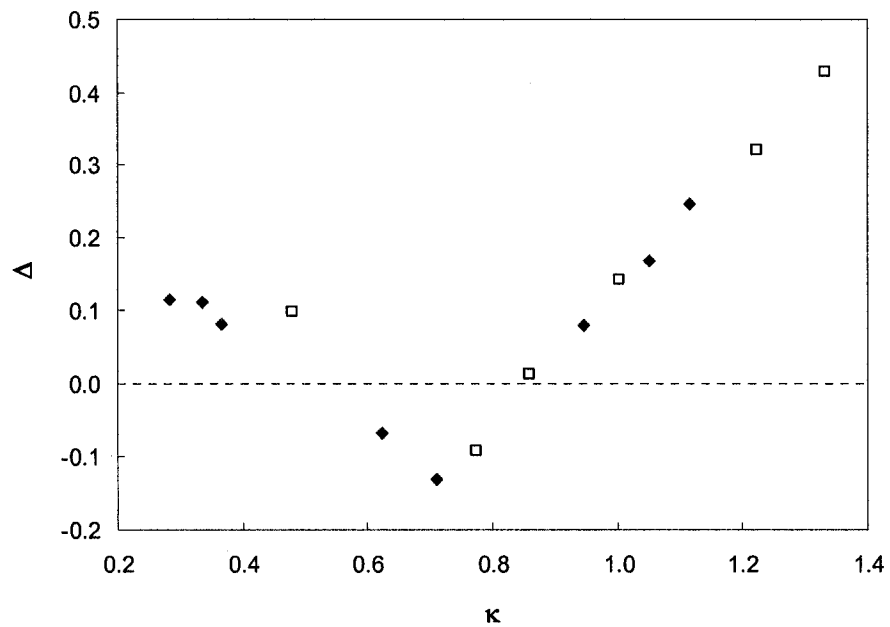


Figure 4.26: The deformation parameter as a function of the dimensionless bubble size for bubbles rising in 0.1% PAM solution in 15 mm square capillary. The open symbols correspond to the bubbles presented in Figure 4.23.

Initially, the bubble shapes are prolate (see Figures 4.24 - 4.26). As the bubble volume increases, the width of the bubble increases faster than the length of the bubble resulting in oblate bubbles that show a pointed cusp at the rear of the bubble. For $\kappa > 0.8$, the bubble reaches its maximum width and any increase in the bubble volume results in an increase in the length of the bubble. For larger bubble volumes ($\kappa > 1$), the bubbles show a negative curvature in the rear of the bubble while maintaining the cusped end. The minimum film thickness for the bubbles rising in PAM1-2 system is shown in Figure 4.27. Similar to Newtonian bulk fluids, the film thickness reduces rapidly and eventually reaches a plateau value.

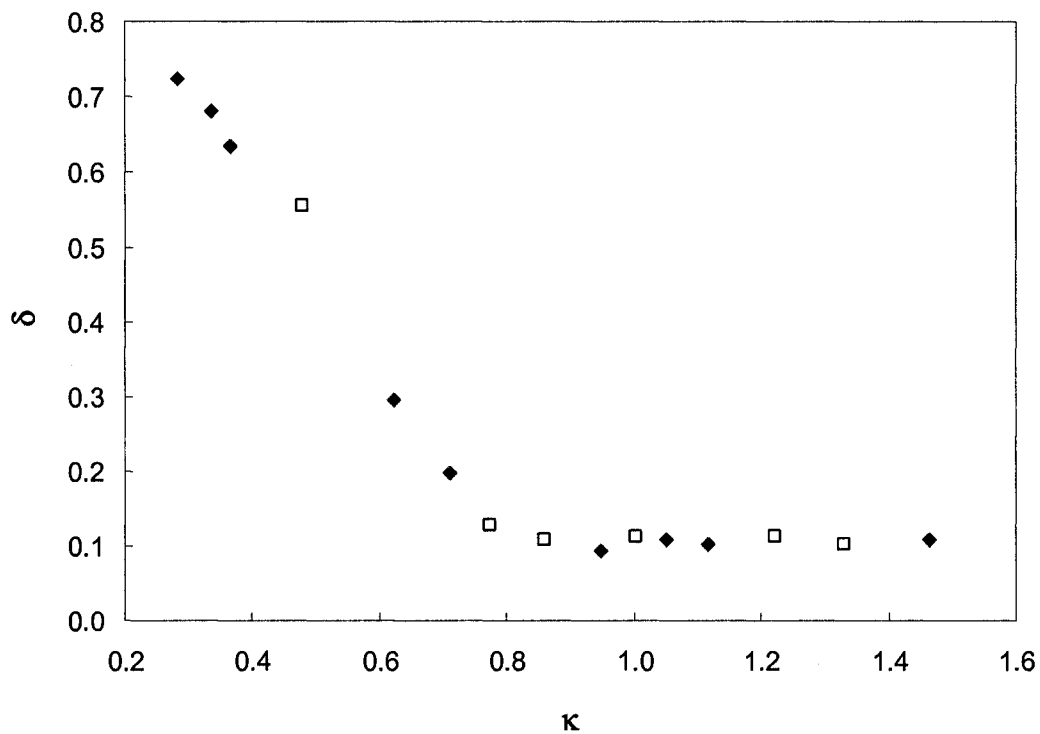


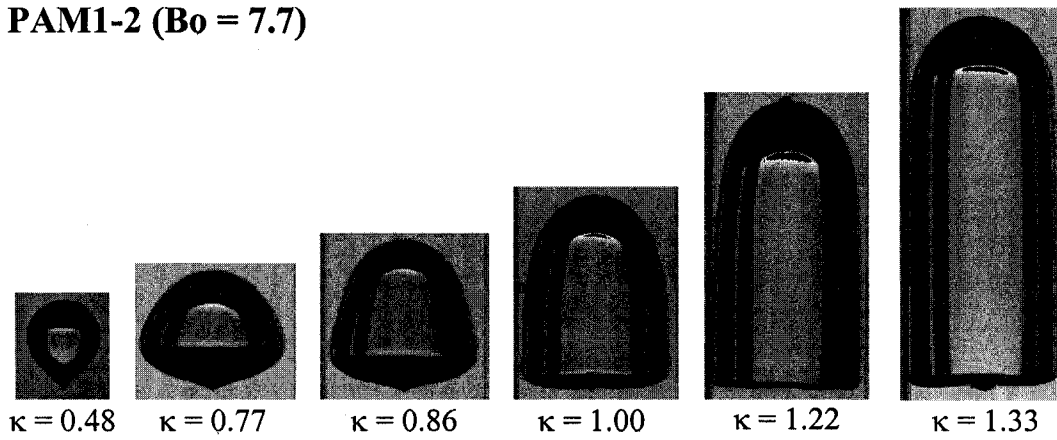
Figure 4.27: The dimensionless film thickness as a function of the dimensionless bubble size for bubbles rising in 0.1% PAM solution in 15 mm square capillary. The open symbols correspond to the bubbles presented in Figure 4.23.

The effect of changing the bulk elasticity of the fluid on the steady shapes of bubbles rising in a 15 mm square capillary is seen in Figure 4.28. A pointed cusp at the trailing edge of the bubble is seen for all the elastic fluids considered. For fluids with a higher bulk viscosity (PAM2-2 and PAM3-2), the negative curvature at the rear of the bubble is not observed. In comparing the shapes obtained for PAM1-2 and PAM2-2, as the elasticity of the fluid is increased, the bubbles become more prolate with more fore and aft symmetry.

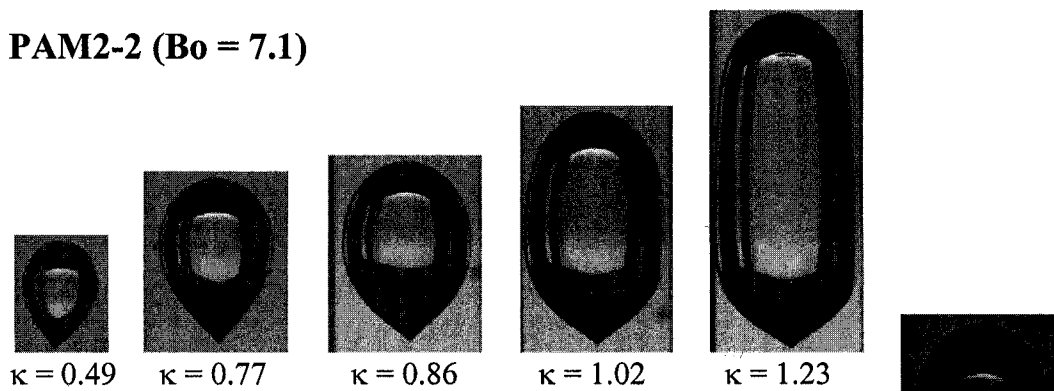
The dimensional velocities for bubbles rising in a 15 mm square capillary filled with 0.1% PAM and 0.25% PAM solutions are shown in Figure 4.29. For small bubbles, as the bubble volume increases, the terminal velocity of the bubble increases due to increased buoyancy. With increasing bubble volume, the wall drag retards the velocity of the bubble and it reaches a plateau value. Beyond a critical bubble size ($V_d = 0.63 \text{ cm}^3$ and $\kappa = 0.71$ for PAM1-2), the bubble velocity is independent of the bubble size similar to a Taylor bubble. The critical bubble volume is consistent with the critical bubble size for a constant film thickness.

The effects of elasticity and the wall can be determined by comparing the velocity of the bubble to the velocity of a spherical bubble of similar volume rising in a Newtonian fluid, U_{HR} . The dimensionless velocity, $U^* = U_d/U_{HR}$, as a function of the bubble volume is shown in Figure 4.30. For the smallest bubble sizes, the bubble velocities are 1.5 - 3 times that of Hadamard-Rybczinski velocity for a spherical bubble of the same volume and the same zero-shear viscosity. The dimensionless velocity, U^* for bubbles rising

PAM1-2 ($Bo = 7.7$)



PAM2-2 ($Bo = 7.1$)



PAM3-2 ($Bo = 9.1$)

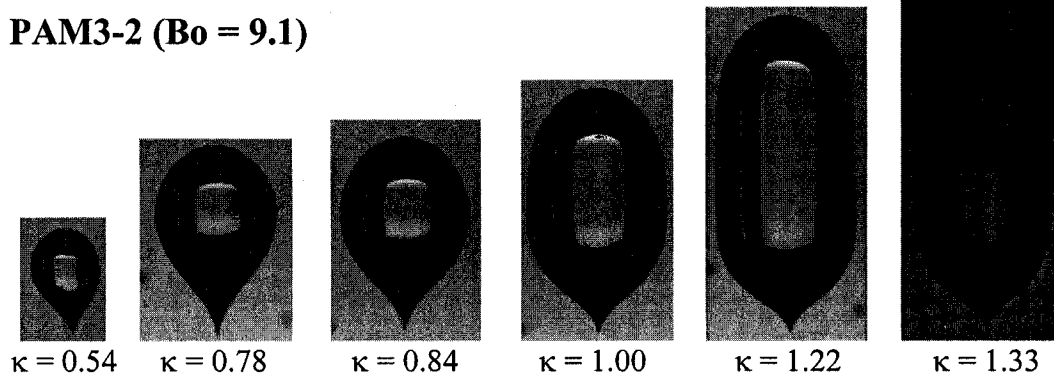


Figure 4.28: Steady shapes for air bubbles as a function of the dimensionless bubble size for air bubbles rising in 0.1% PAM, 0.25% PAM, and 0.1% PAM in 50% glycerol-water solutions.

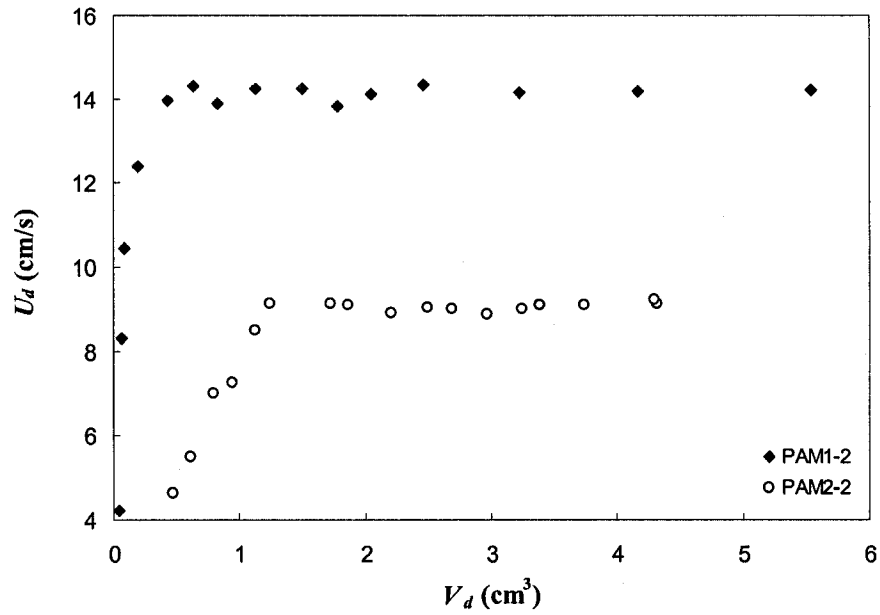


Figure 4.29: Comparison of terminal velocity as a function of the bubble volume for air bubbles rising in 15 mm square capillary filled with 0.1% PAM (PAM1-2) and 0.25% PAM (PAM2-2) solutions.

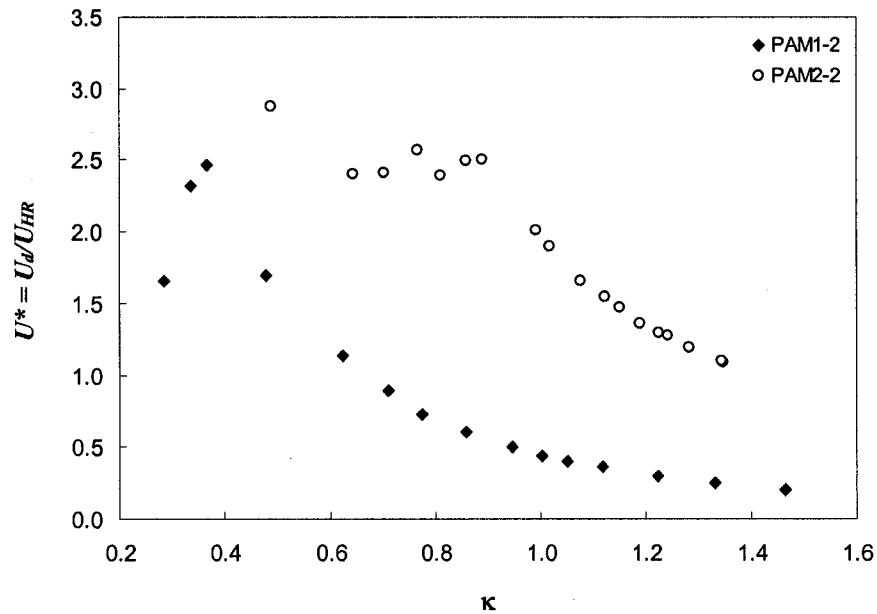


Figure 4.30: Comparison of steady dimensionless velocity of air bubbles as a function of the bubble size for air bubbles rising in 15 mm capillary filled with 0.1% PAM (PAM1-2) and 0.25% PAM (PAM2-2) solutions..

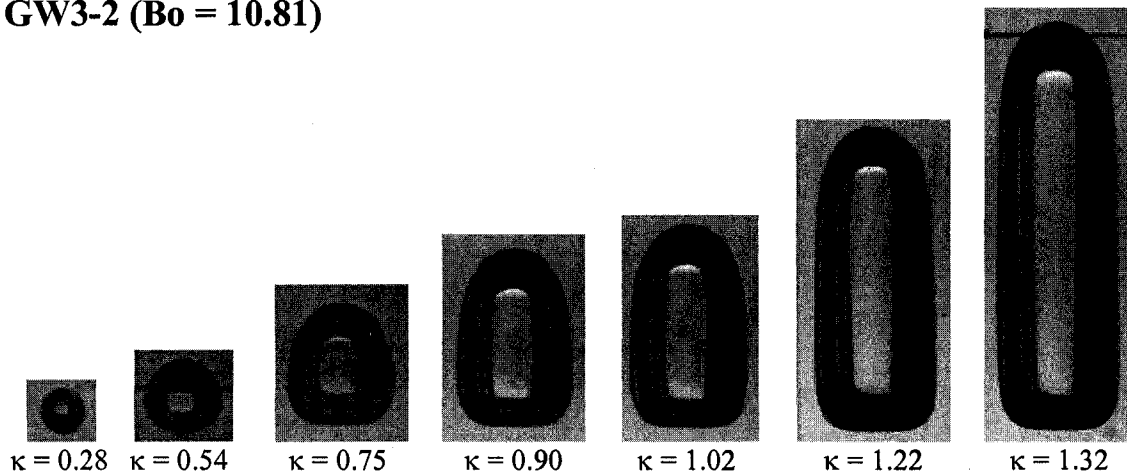
in Newtonian fluids showed that even for small bubbles, the terminal velocity of the bubbles is much lower than U_{HR} . The increased bubble velocity for bubbles translating in elastic fluids may be attributed to the shear-thinning behavior of the elastic fluids.

Surfactant Systems

A comparison of the steady bubble shapes obtained for bubbles rising in a 15 mm square capillary filled with 95% glycerol-water solution in the absence (GW3-2) and presence of 10 ppm of Triton X-100 surfactant (TX1-2) is shown in Figure 4.31. The length, width, shape, and the deformation parameter for the bubbles for GW3-2 and TW1-2 systems are shown in Figures 4.32 - 4.34. Figure 3.6 shows that the presence of 10 ppm of Triton X-100 does not affect the equilibrium surface tension of 95% glycerol-water-air interface. Therefore, any differences observed between the dynamics of bubbles in GW3-2 and TX1-2 systems are due to the non-equilibrium effects as surfactant molecules redistribute along the interface of the bubble as the bubble translates. Very small bubbles are nearly spherical and the presence of surfactants does not seem to affect the shape of the smaller bubbles. However, for larger bubble volumes in the presence of surfactants, the length of the bubble is higher and the width of the bubble is lower than the surfactant-free bubble. The bubbles in the presence of surfactants are more prolate as compared to the bubbles with small amounts of surfactant consistent with the observation of Almatroushi and Borhan [2]. As a consequence, the minimum dimensionless film thickness for the bubbles with small amounts of surfactants is higher than the film thickness in the absence

of surfactants although this difference is very small (see Figure 4.35). This observation is consistent with the earlier investigations [18,20].

GW3-2 ($Bo = 10.81$)



TX1-2 ($Bo = 10.72$)

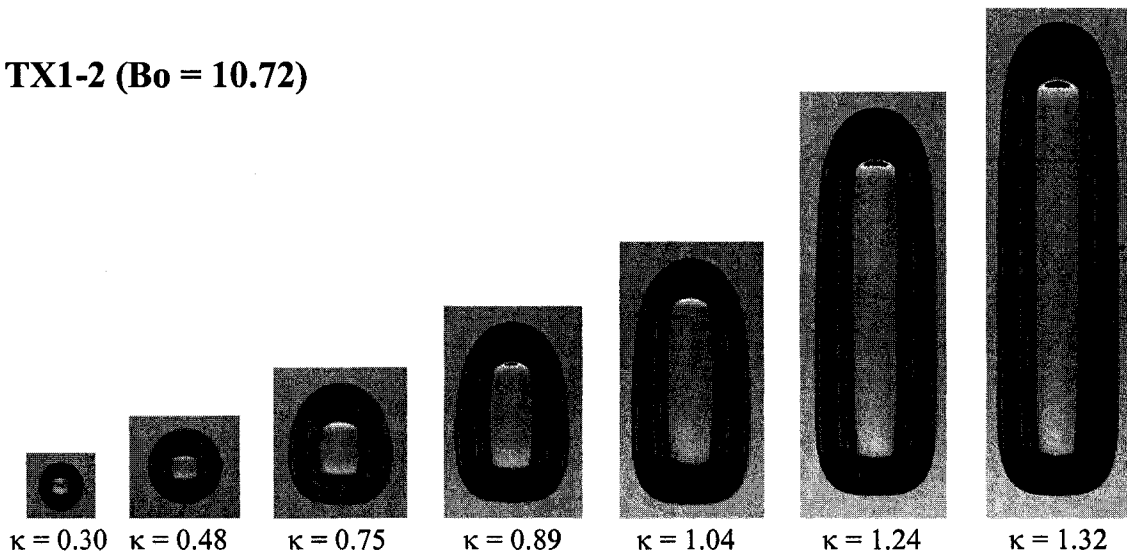


Figure 4.31: Steady shapes for air bubbles as a function of the dimensionless bubble size for air bubbles rising in 95% glycerol-water solution (GW3-2) and 95% glycerol-water solution with 10 ppm Triton X-100 (TX1-2) in 15 mm square capillary.

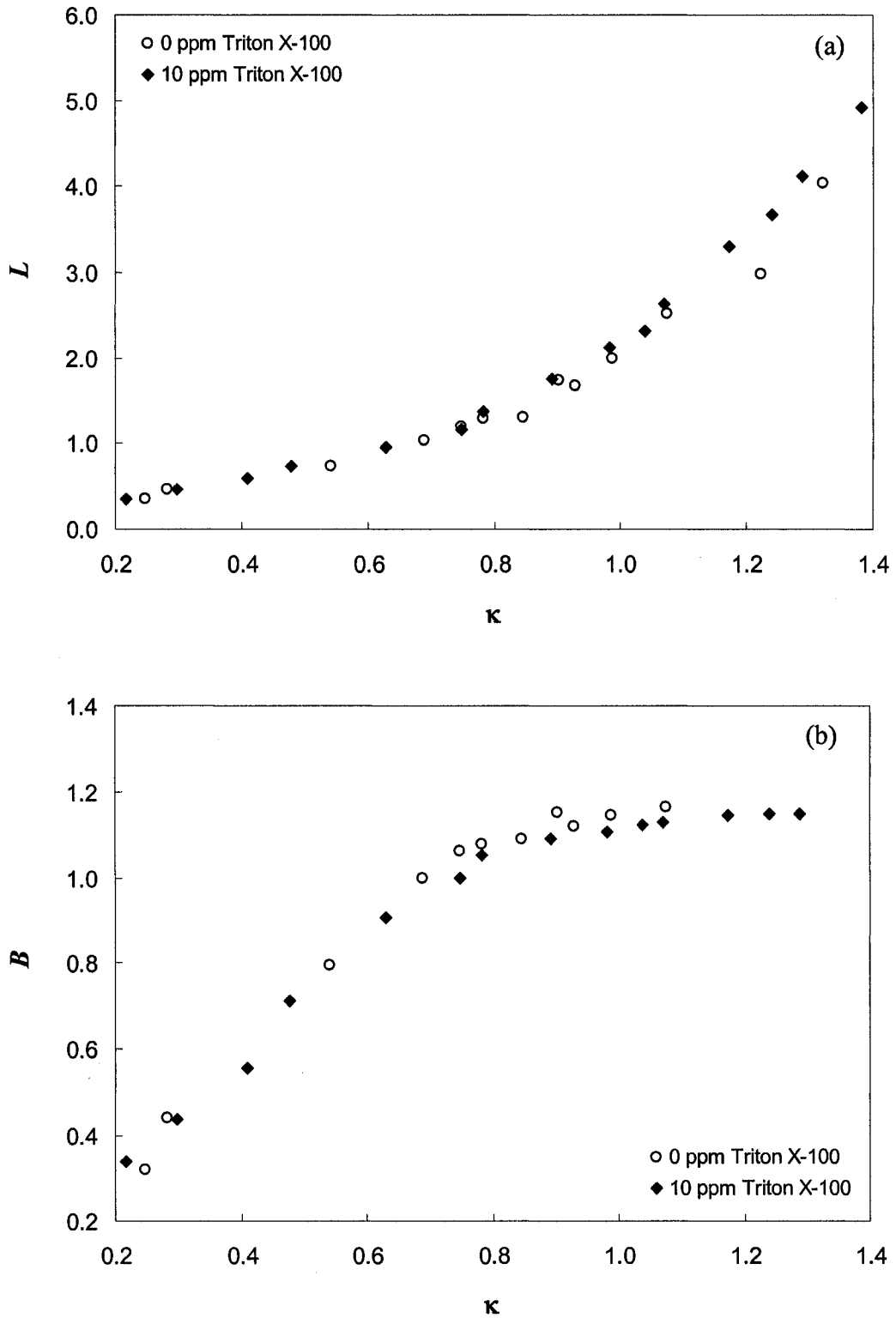


Figure 4.32: The (a) length and (b) width of bubbles as a function of bubble size for bubbles in GW3-2, TX1-2, and TX3-2 systems in 15 mm square capillary.

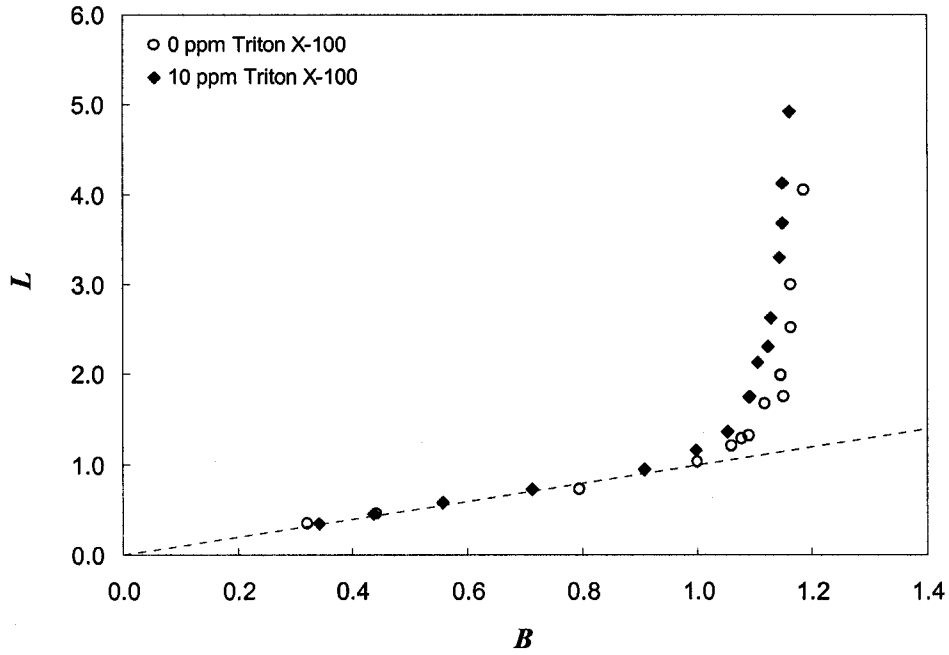


Figure 4.33: The length of the bubble as a function of the bubble width for bubbles in GW3-2, TX1-2, and TX3-2 systems in 15 mm square capillary. The dashed line represents the curve for a spherical bubble.

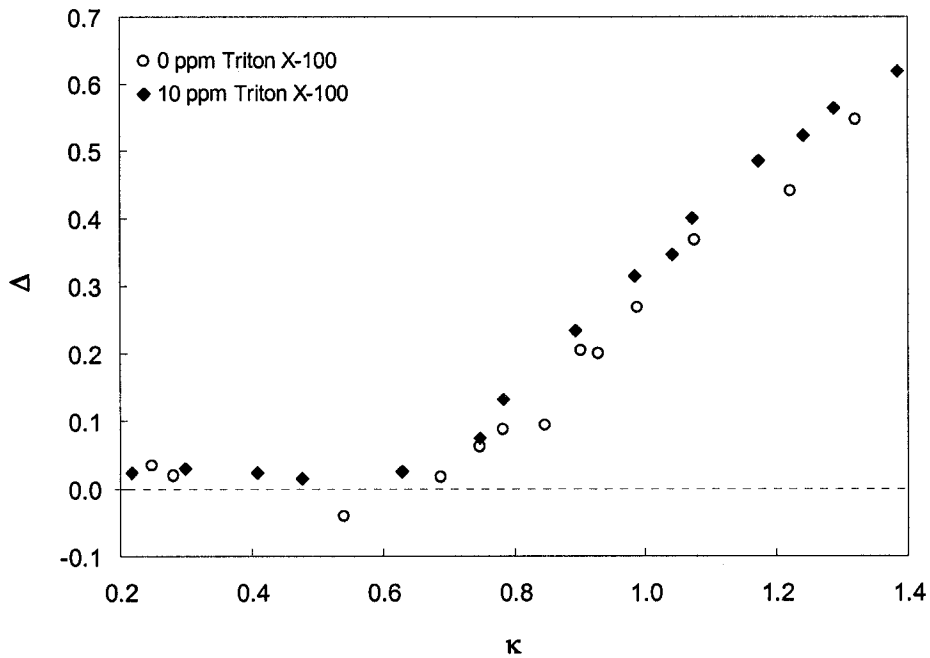


Figure 4.34: The deformation parameter as a function of the dimensionless bubble size for bubbles in GW3-2, TX1-2, and TX3-2 systems in 15 mm square capillary.

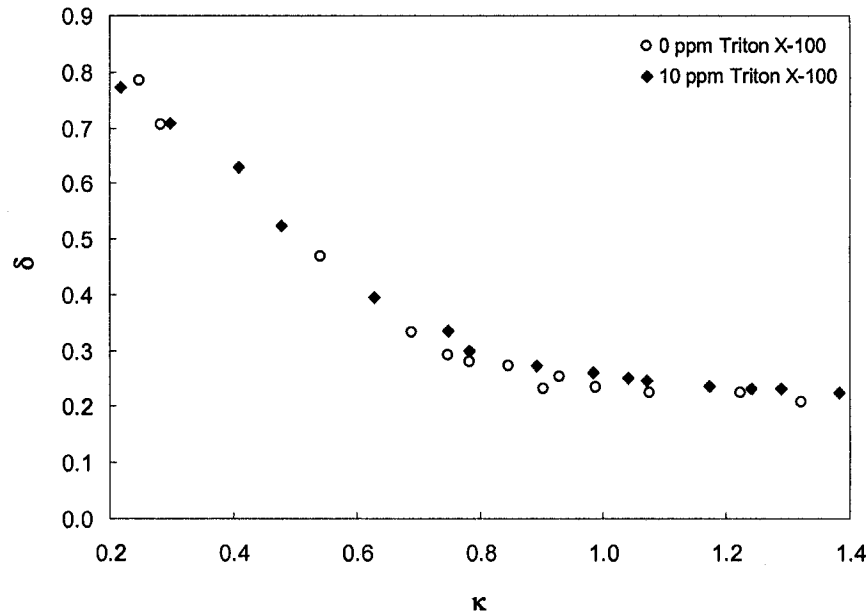


Figure 4.35: Comparison of the dimensionless film thickness as a function of the bubble size for bubbles in GW3-2, TX1-2, and TX3-2 systems in 15 mm square capillary.

The dimensional terminal velocity as a function of bubble volume for 0 ppm, 10 ppm, and 1000 ppm of Triton X-100 in 95% glycerol-water is shown in Figure 4.36. In the absence of surfactants, the bubble velocity increases with bubble volume for small bubble volumes due to predominantly buoyancy effects. With increasing wall drag, the velocity reduces and reaches a plateau value. In the presence of very small amounts of surfactants (10 ppm), the characteristics of the velocity-volume curve remains the same. However, the magnitude of the velocity decreases to about 70% of the surfactant-free velocity. For bubbles rising in confined domains, the fluid flow along the interface is from the front stagnation point to the rear stagnation point. Thus, surfactants accumulate at the rear of the bubble reducing the surface tension there. The gradient in surface tension along the interface generates Marangoni stresses causing a tangential flow from the rear of the

bubble (low surface tension region) to the front of the bubble (high surface tension region). The Marangoni flow opposes the bulk fluid flow and reduces the terminal velocity of the bubble. As the surfactant concentration is increased, the steady bubble velocity for long bubbles increases. Triton X-100 is known to have strong desorption kinetics [29]. Therefore, at higher surfactant concentrations, the surfactant transport to the interface is very fast. This reduces the surfactant gradients along the interface, reducing the Marangoni stresses and remobilizing the interface. At 1000 ppm Triton X-100 concentration, the interface is completely mobilized and the terminal velocity of long bubbles is the same as the terminal velocity of long bubbles in the absence of surfactants.

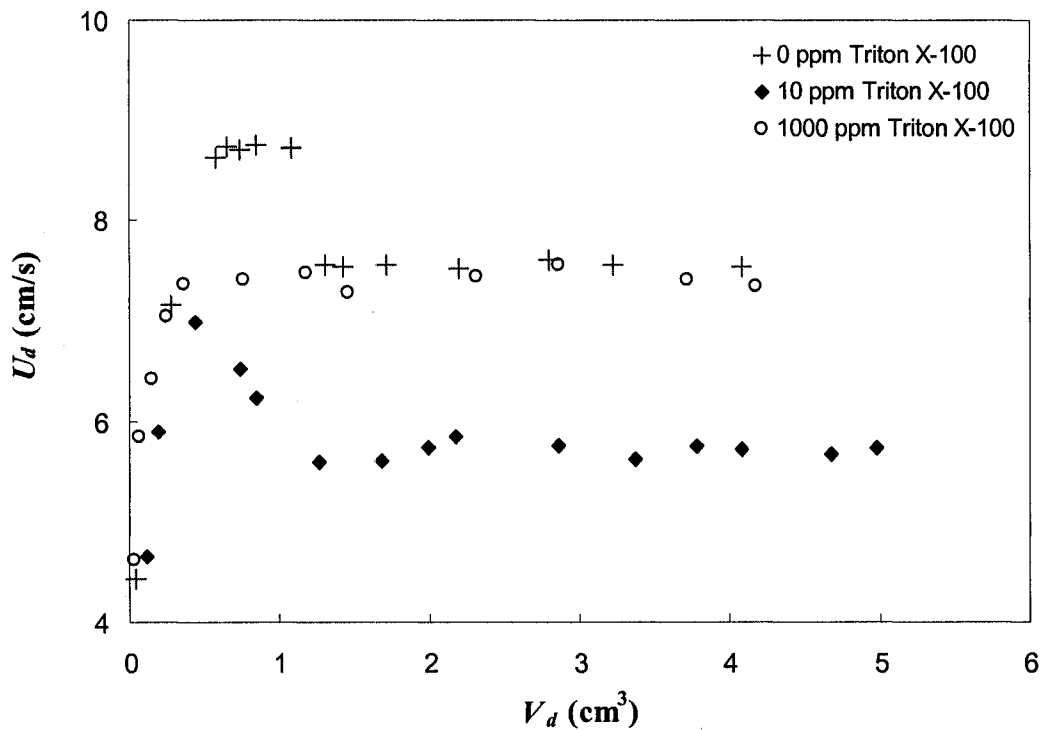


Figure 4.36: Comparison of terminal velocity as a function of the bubble volume for air bubbles in GW3-2, TX1-2, and TX3-2 systems.

The dimensionless velocity, $U^* = U_d/U_{HR}$, as a function of the bubble volume for varying surfactant concentrations is shown in Figure 4.38. For the smallest bubble with $\kappa = 0.25$ the bubble velocity is about 50% of the Hadamard-Rybczinski velocity for a spherical bubble of the same volume. The reduction in the bubble velocity is due to the wall drag. In the presence of very small amount of surfactant (10 ppm), the terminal velocity of small bubbles is about 15% of the Hadamard-Rybczinski velocity for a spherical bubble of the same volume. With increasing surfactant concentration, the bubble interface gets mobile and the dimensionless velocity increases.

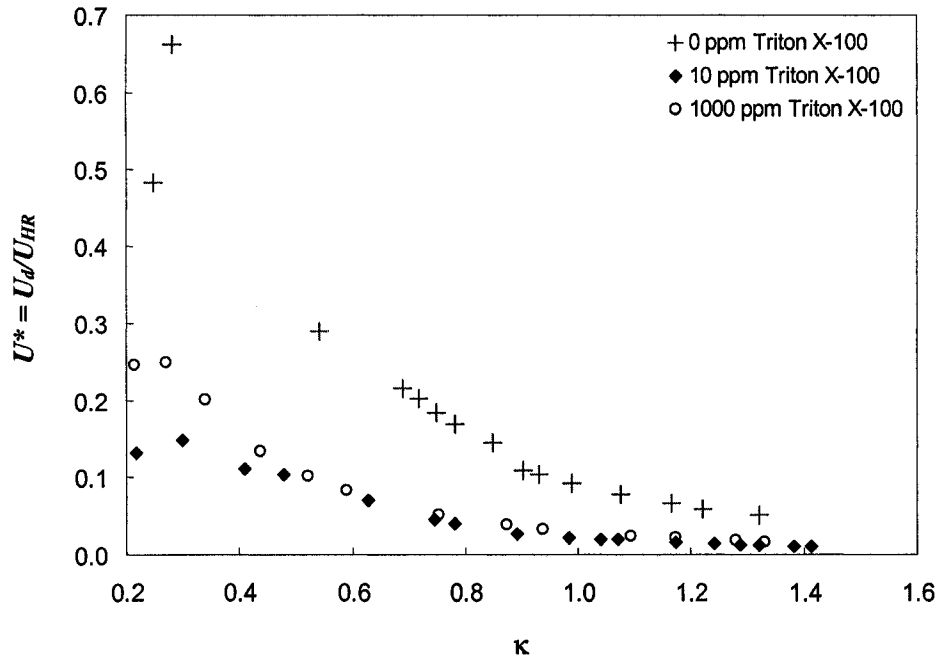


Figure 4.37: Comparison of steady dimensionless velocity of air bubbles as a function of the bubble size for GW3-2, TX1-2, and TX3-2 systems.

CHAPTER V

SUMMARY AND FUTURE WORK

In this thesis the motion of air bubbles in square capillaries moving under the influence of gravity was studied at finite Reynolds numbers. The bubbles were injected into vertical square capillaries filled with the bulk fluid and imaged using a CCD camera connected to a computer. The steady shape, deformation, film thickness, and velocity of the bubbles as a function of the bubble size were determined from the captured images and image analysis software. The bulk fluid phase was either Newtonian, viscoelastic, or a surfactant solution. The effect of changing the bulk fluid viscosity, elasticity, capillary size, and surfactant concentration on the dynamics of the bubbles was investigated.

Bubbles rising in a Newtonian fluid are nearly spherical at lower bubble volumes. As the bubble volume increases, the bubbles become prolate and lose their fore and aft symmetry. If the viscosity of the bulk fluid phase is reduced, the air bubbles develop a negative curvature at the rear of bubbles. The critical viscosity at which the shape transition occurs depends on the size of the capillary. As the capillary size increases, the critical viscosity at which the reentrant cavity is observed increases. The terminal velocity of the bubbles increases with volume for small bubble volumes. As the bubble

size becomes comparable to the capillary size, the increased wall drag reduces the velocity of the bubbles showing a local maximum in the velocity-volume curve. Beyond a critical bubble volume, the bubble velocity is independent of the bubble size similar to a Taylor bubble. For bubbles in smaller capillaries, the local maximum in the velocity-volume curve disappears and the steady velocity of the bubbles increases monotonically with bubble volume.

For bubbles rising in a viscoelastic fluid, a pointed cusp is seen at the trailing edge of the bubbles similar to the cusps observed for bubbles rising in a quiescent viscoelastic fluid. The cusp shape appears to be axisymmetric for all the fluids considered. The reentrant cavity along with the cusp is observed as the viscosity of the bulk phase is reduced. The minimum film thickness between the bubble wall and the tube wall reduces as the bubble volume increases and reaches a limiting value for long bubbles. The terminal velocities for bubbles rising in the viscoelastic fluids studied increases monotonically with bubble volume and reaches a plateau value. The steady bubble velocities are much higher than that for an equivalent bubble moving in quiescent Newtonian fluid with the same zero shear viscosity. This is due to the shear-thinning effect of the viscoelastic fluids.

In the presence of very small amounts of surfactants, differences in the dynamics of bubble motion are observed due to non-equilibrium effects. The bubbles in the presence of surfactants are more prolate than the corresponding bubbles in the absence of surfactants. These results are consistent with the observations of surfactant effects on the rise of bubbles in cylindrical capillaries. The surfactants are adsorbed at the air-liquid

interface. As the bubble rises in the square capillary, surfactants accumulate at the rear of the bubble setting up surface tension gradients along the length of the bubble. The Marangoni stresses thus generated reduce the terminal velocity of the bubbles even for very small amounts of surfactants added to the systems. As the surfactant concentration is increased, the surfactant (Triton X-100) adsorbs quickly at the air-liquid interface and remobilizes the interface. The terminal velocity of long bubbles with 1000 ppm Triton X-100 concentration is the same as the terminal velocity of long bubbles in the absence of surfactants.

The motion of bubbles in square capillaries is a relevant problem due to its applications in the field of microfluidics. The results of this thesis are a first attempt at characterizing motion of finite bubbles in non-circular channels in the presence of elastic and surfactant effects. Several future research projects have been identified as an outcome of this thesis and will further our understanding of two-phase flows in confined domains. These include:

- Studying bubble dynamics for a wider range of Bond, capillary, and Reynolds numbers.
- Investigating the effect of non-zero density and viscosity of the drop fluid.
- Determining the effects of bubble dynamics at the microscale.
- Studying surfactants with different adsorption-desorption kinetics.
- Investigating the effects of other shear-thinning inelastic and elastic fluids.

REFERENCES

1. Acharya, A.; Mashelkar, R.A.; Ulbrecht, J. Mechanics of bubble motion and deformation in non-Newtonian media. *Chem. Engg. Sci.* **32**, 863-872, 1976.
2. Almatroushi, E.; Borhan, A. Surfactant Effect on the buoyancy-driven motion of bubbles and drops in the tube. *Ann. N.Y. Acad. Sci.*, **1027**, 330-341, 2004.
3. Astarita, G.; Apuzzo, G. Motion of gas bubbles in non-Newtonian liquids. *AIChE J.* **11**, 815-820, 1965.
4. Bird, R.A.; Armstrong, R.C.; Hassager, O. Dynamics of polymeric liquids: Fluid Mechanics, Wiley, New York, vol. 1, 1987.
5. Borhan, A.; Pallinti, J. Buoyancy driven motion of viscous drops through cylindrical capillaries at small Reynolds numbers. *Ind. Eng. Chem. Res.*, **34**, 2750-2761, 1995.
6. Bretherton, F.P. The motion of long bubbles in tubes. *J. Fluid Mech.*, **10**, 166-188, 1961.
7. Clanet, C.; Héraud, P.; Searby, G. On the motion of bubbles in vertical tubes of arbitrary cross-sections: some complements to the Dumtrescu-Taylor problem. *J. Fluid Mech.*, **519**, 359-376, 2004.
8. Deng, P.; Lee, Y.; Cheng P. Micro bubble dynamics in DNA solutions. *J. of Micromechanics and Microengineering.* **14**, 693-701, 2004.
9. Hassager, O. Negative wake behind bubbles in non-Newtonian liquids. *Nature*, **279**, 402-403, 1979.

10. Hazel, A. L.; Heil, M. The steady propagation of a semi-infinite bubble into a tube of elliptical or rectangular cross-section. *J. Fluid Mech.*, **470**, 91-114, 2002.
11. Herrera-Velarde, J.R.; Zenit, R.; Chehata, D.; & Mena, B. The flow of non-Newtonian fluids around bubbles and its connection to the jump discontinuity. *J Non-Newtonian Fluid Mech*, , **111**, 199-209, 2003.
12. Kolb, W.B.; Cerro, R.L. Coating the inside of a capillary of square cross section. *Chem. Eng. Sci.*, **46**, 2181-2195, 1991.
13. Kolb, W.B.; Cerro, R.L. Film flow in the space between a circular bubble and a square tube. *J. Colloid Interface Sci.*, **159**, 302-311, 1993.
14. Kolb, W.B.; Cerro, R.L. The motion of long bubbles in tubes of square cross section. *Phys. Fluids A*, **5**, 1549-1557, 1993.
15. Leal, L.G.; Skoog, J.; Acrivos, A. On the motion of gas bubbles in viscoelastic liquid. *Can. J. Chem. Engng* , **49**, 569-575, 1971.
16. Liu, Y.J.; Liao, T.Y.; & Joseph, D.D. A two dimensional cusp at the trailing edge of an air bubble rising in a viscoelastic liquid. *J. Fluid Mech.*, **304**, 321-342, 1995.
17. Olbricht, W.L. Pore-scale prototypes of multiphase flow in porous media. *Annu. Rev. Fluid Mech.*, **28**, 187-214, 1996.
18. Park, C.-W. Influence of soluble surfactants on the motion of a finite bubble in a capillary tube. *Phys. Fluids A*, **4**, 2335-2347, 1992.
19. Ratulowski, J.; Chang, H.-C. Transport of gas bubbles in capillaries. *Phys. Fluids A*, **1**, 1642-1655, 1989.
20. Ratulowski, J.; Chang, H.-C. Marangoni effects of trace impurities on the motion of long gas bubbles in capillaries. *J. Fluid Mech.*, **210**, 303-328, 1990.

21. Reinelt, D.A. The rate at which long bubble rises in a vertical tube. *J. Fluid Mech.*, **175**, 557-565, 1986.
22. Rodrigue, D.; Blanchet, J.F.. Recent developments on the velocity-volume bubble jump discontinuity. *Congr. on Rheology*, **14**, 2004.
23. Rodrigue, D.; De Kee, D. Bubble velocity jump discontinuity in polyacrylamide solutions: a photographic study. *Rheol Acta* , **38**, 177, 1999.
24. Rodrigue, D.; De Kee, D.; Chan Man Fong, C. An experimental study of the effect of surfactants on the free rise velocity of gas bubbles. *J Non-Newtonian Fluid Mech.*, **66**, 213-232, 1996.
25. Rodrigue, D.; De Kee, D.; Chan Man Fong, C.F.. Bubble velocities: further developments on the jump discontinuity. *J. Non-Newtonian Fluid Mech.*, **79**, 45-55, 1998.
26. Sousa, R.G.; Nogueira, S.; Pinto, A.M.F.R.; Reithmuller, M.L.; Campos, J.B.L.M. Flow in the negative wake of a Taylor bubble rising in viscoelastic carboxymethylcellulose solutions: particle image velocimetry measurements. *J. Fluid Mech.*, **511**, 217-236, 2004.
27. Sousa, R.G.; Reithmuller, M.L.; Pinto, A.M.F.R.; Campos, J.B.L.M. Flow around individual Taylor bubbles rising in stagnant CMC solutions: PIV measurements. *Chem. Eng. Sci.* **60**, 1859-1873, 2005.
28. Sousa, R.G.; Reithmuller, M.L.; Pinto, A.M.F.R.; Campos, J.B.L.M. Flow around individual Taylor bubbles rising in stagnant polyacrylamide (PAA) solutions. *J. non-Newtonian fluids.* **135**, 16-31, 2006.

29. Stebe, K.J.; Lin, S.Y.; Maldarelli, C. Remobilizing surfactant retarded fluid particle interfaces.I. Stress-free conditions at the interfaces of micellar solutions of surfactants with sorption kinetics. *Phys. Fluids*, **3**, 10003-10020, 1991.
30. Stebe, K.J.; Lin, S.Y.; Maldarelli, C. Remobilizing surfactant retarded fluid particle interfaces-II.Controlling the surface mobility at interfaces of solutions containing surface active components. *J. Colloid Interface Sci.*,**163**, 177-189, 1994.
31. Taha, T.; Cui, Z.F. CFD modeling of slug flow inside square capillaries. *Chem. Eng. Sci.*, **61**, 665-675, 2006.
32. Wong, H.; Radke, C.J.; Morris, S. The motion of bubbles in polygonal capillaries. Part 1. Thin films. *J. Fluid Mech.*, **292**, 71-94, 1995.
33. Wong, H.; Radke, C.J.; Morris, S. The motion of bubbles in polygonal capillaries. Part 2. Drag, fluid pressure and fluid flow. *J. Fluid Mech.*, **292**, 95-110, 1995.

APPENDIX

C-program to calculate the bubble volume from r-z data.

```
#include<stdio.h>
#include<math.h>
#define max 1000
main()
{
    int i,n;
    float f[max],r[max],z[max],pi,I;
    I=0.0;
    pi=3.14;
    n=33;
    FILE *fpa;
    fpa=fopen("drop14.txt","r");
    for(i=1;i<=n;i++)
    {
        fscanf(fpa,"%f",&r[i]);
        fscanf(fpa,"%f",&z[i]);
    }
    fclose(fpa);
    for(i=1;i<=n;i++)
    {
        f[i]=pi*r[i]*r[i];
    }
    for(i=1;i<=n-1;i++)
    {
        I=I+(f[i]+f[i+1])/2.0*(z[i]-z[i+1]);
    }
    printf("\n The Volume obtained = %f\n",I/1000000000000);
}
```